Comparative Degradation Analysis of (NMC/LTO) and Hybrid (NMC/Gr, NMC/LTO) Battery Packs for V2X Application

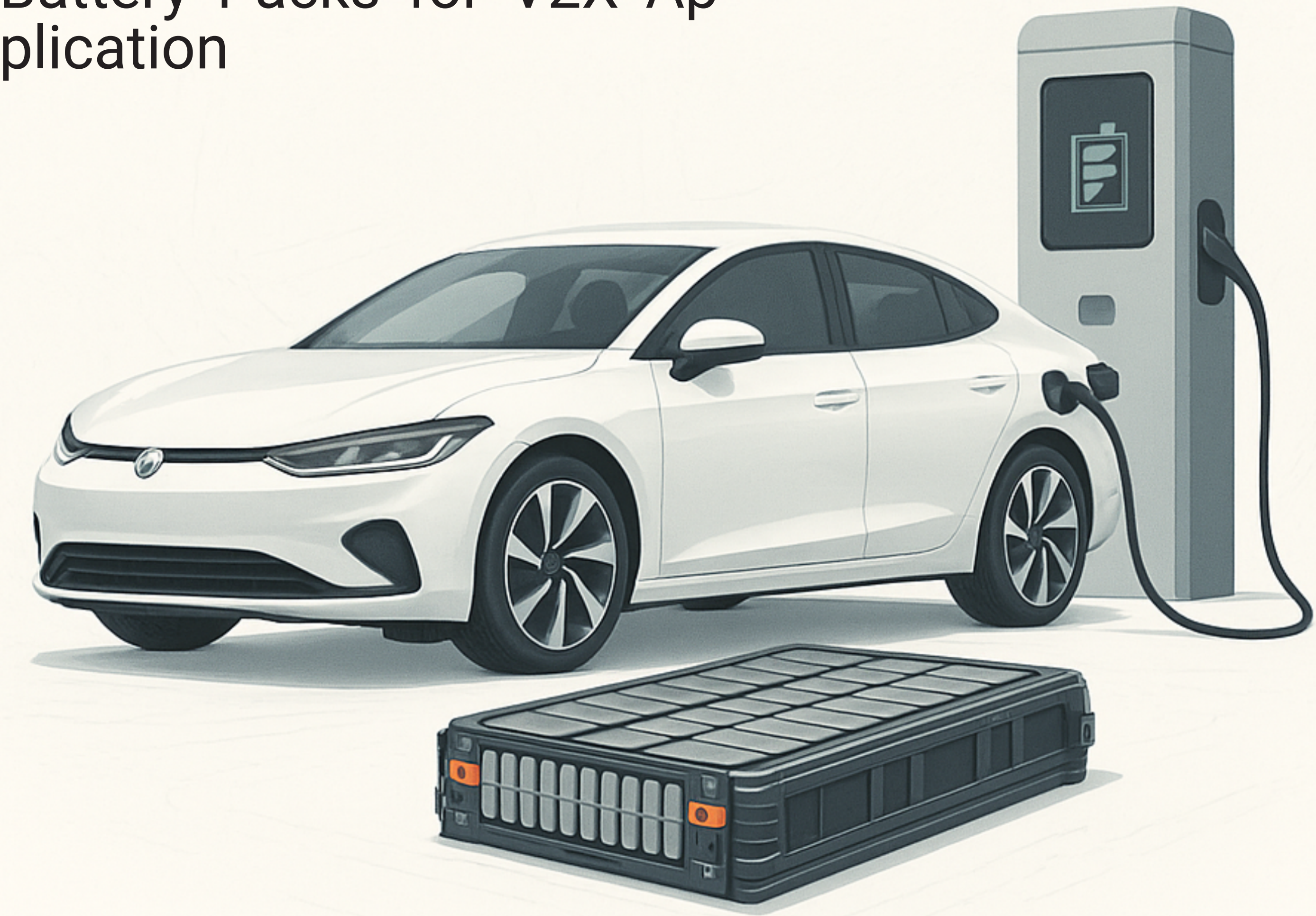

TUDelft

Comparative Degradation Analysis of (NMC/LTO) and Hybrid (NMC/Gr,NMC/LTO) Battery Packs for V2X Application

Degradation Modeling of (NMC/LTO) and Hybrid (NMC/Gr,NMC/LTO) Battery packs with Subsequent Comparative Evaluation Versus Conventional (NMC/Gr) and (LFP/Gr) Systems Under Driving and Vehicle-to-Grid (V2G) Operating Conditions

by

Hamza Alrez

Student number 5611644

To obtain the degree of Master of Science in Sustainable Energy Technology
at the Delft University of Technology

Supervisor Dr.ir.: Gautham Ram Chandra Mouli

Thesis committee

Dr.ir. Gautham Ram Chandra Mouli
Dr.ir. Moumita Rana
Dr.ir. Wenli Shi

Abstract

The increasing penetration of renewable energy sources in modern power systems is essential to achieve sustainable energy transitions; however, their inherent intermittency continues to pose challenges to system reliability and operational stability. Energy storage systems are therefore indispensable, and lithium-ion batteries are emerging as a key technology because of their high efficiency, favorable energy density, and widespread deployment. As lithium-ion batteries are increasingly utilized in electric vehicles and grid-integrated applications, accurate modeling of battery degradation has become critical for assessing long-term performance and economic feasibility. Vehicle-to-Grid (V2G) operation, which enables bidirectional power exchange between electric vehicles and the grid, offers significant system-level benefits but introduces additional battery cycling and operating stress.

This study presents a two-year simulation framework to investigate lithium-ion battery degradation under driving and combined driving–V2G operations. A comparative analysis is conducted across multiple battery chemistries, including nickel–manganese–cobalt (NMC/Graphite), lithium iron phosphate (LFP/Graphite), lithium titanate oxide (NMC/LTO) and a hybrid configuration combining (NMC/Graphite) and (NMC/LTO) batteries. An empirical degradation model for the (NMC/LTO) battery is developed and validated using experimental data available in the literature. Degradation models for (NMC/Graphite) and (LFP/Graphite) batteries are adopted from existing studies. In addition, a hybrid degradation model combining NMC and LTO chemistries is introduced to investigate the potential advantages of hybrid battery architectures. Battery power profiles derived from the Worldwide Harmonized Light Vehicles Test Procedure (WLTP) driving cycle are used to represent both conventional driving and V2G-enabled operation. Three simulation scenarios are considered: a baseline driving scenario, a V2G operation scenario, and a sensitivity analysis scenario evaluating the influence of increasing the share of (NMC/LTO) in the hybrid configuration.

The results validate the empirical degradation model developed for the (NMC/LTO), and (NMC/Graphite and NMC/LTO), demonstrating good agreement with the observed long-term aging behavior. A comparative analysis with conventional (NMC/ Graphite) and (LFP/Graphite) chemistries revealed that LTO-based and hybrid configurations exhibit enhanced degradation resistance under normal operating conditions and V2G operation.

Acknowledgment

I want to express my sincere gratitude to my supervisor, Dr.ir. Gautham Ram Chandra Mouli, for his continuous guidance, insightful feedback, and support throughout this thesis. His expertise and encouragement were invaluable during the development of this research. I would also like to sincerely thank my daily co-supervisor, Koen Linders, for his valuable guidance, helpful discussions, and continuous support during this work. His practical insights and feedback greatly contributed to the progress of this research. I would also like to thank the members of my thesis committee, Dr.ir. Moumita Rana and Dr.ir. Wenli Shi, for their time and valuable comments. Finally, I would like to express my appreciation to my family and friends for their constant support and encouragement throughout my studies.

Contents

List of Figures

List of Tables

List of Abbreviations

Abbreviation	**Meaning**
BEV	Battery Electric Vehicle
cd	Cycle Depth
CEI	Cathode Electrolyte Interphase
CL	Conductivity Loss
cr	Current Rate
DoD	Depth of Discharge
ECM	Equivalent Circuit Model
EM	Empirical Model
EOL	End-of-Life
EV	Electric Vehicle
FEC	Full Equivalent Cycles
Gr	Graphite
LAM	Loss of Active Material
LCO	Lithium Cobalt Oxide ($LiCoO_2$)
LFP	Lithium Iron Phosphate ($LiFePO_4$)
LIB	Lithium-Ion Battery
LLI	Loss of Lithium Inventory
LMO	Lithium Manganese Oxide ($LiMn_2O_4$)
LTO	Lithium Titanate Oxide ($\mathrm{Li_4Ti_5O_{12}}$)
MLM	Machine Learning Model
NCA	Lithium Nickel Cobalt Aluminium Oxide ($LiNi_xCo_yAl_zO_2$)
NMC	Lithium Nickel Manganese Cobalt Oxide ($LiMn_xNi_yCo_zO_2$)
PBM	Physics-Based Model
RES	Renewable Energy Sources
SEI	Solid Electrolyte Interphase
SoC	State of Charge
SoH	State of Health

V2G	Vehicle-to-Grid
V2X	Vehicle-to-Anything
WLTP	Worldwide Harmonized Light Vehicles Test Procedure

1

Introduction

The global energy sector is undergoing a profound transformation driven by the need to reduce greenhouse gas emissions, limit environmental impacts, and reduce dependence on finite fossil fuel resources. Renewable energy sources such as wind and solar power are central to this transition; however, their large-scale integration is constrained by inherent intermittency and variability. Ensuring the reliable and stable operation of power systems with high renewable penetration, therefore, requires effective energy storage solutions.

Among the wide range of available energy storage technologies—including pumped hydroelectric storage, compressed air energy storage, hydrogen systems, and thermal storage—battery energy storage systems have gained particular attention. Their modularity, fast response, and operational flexibility make them suitable for stationary and mobile applications. Within this category, lithium-ion batteries have become the dominant technology due to their high energy density, long cycle life, and ongoing cost reductions driven by technological advances and large-scale manufacturing.

Lithium-ion batteries play a central role in the electrification of transportation, where electric vehicles demand high performance, efficiency, and durability. At the same time, increasing electricity demand and the growing share of renewable generation have motivated the development of Vehicle-to-Anything (V2X) technologies. In particular, Vehicle-to-Grid (V2G) operation enables electric vehicles to exchange power with the electricity grid, allowing them to provide services such as peak shaving, frequency regulation, and balancing renewable energy. By aggregating the storage capacity of electric vehicles, V2G can enhance grid flexibility and reduce infrastructure requirements. Despite these advantages, concerns regarding battery degradation remain a major barrier to the widespread adoption of V2G systems [1]. Bidirectional power flow, increased energy throughput, and more frequent cycles introduce additional stress on the battery, potentially accelerating capacity fade and reducing overall lifetime [2]. Battery degradation directly affects vehicle performance, user acceptance, and the economic viability of V2G participation. As a result, a detailed understanding of degradation mechanisms under realistic driving and V2G operating conditions is essential. Battery aging behavior is strongly influenced by cell chemistry, operating conditions, and cycling characteristics. Conventional lithium-ion chemistries such as nickel–manganese–cobalt (NMC) and lithium iron phosphate (LFP) have been extensively studied; however, alternative chemistries such as lithium titanate oxide (LTO) have received comparatively less attention, particularly in the context of real-world and V2G operation. LTO batteries are characterized by exceptional cycle life, high power capability, and enhanced safety, suggesting potential advantages for grid-interactive applications despite their lower energy density. In addition, hybrid battery configurations that combine high-energy and high-power chemistries may offer a practical compromise between performance and degradation.

Against this background, the objective of this work is to investigate battery degradation in electric vehicles operating under both conventional driving and Vehicle-to-Grid (V2G) conditions using a modeling-based approach. The study aims to:

- develop an empirical degradation model for lithium titanate oxide (NMC/LTO) battery configurations.
- propose and model a hybrid (NMC/Graphite, NMC/LTO) battery configuration.
- develop a simulation framework that integrates realistic vehicle driving profiles with battery operation under vehicle-to-grid (V2G) conditions;
- Comparison of degradation behavior across different lithium-ion battery chemistries, including NMC/Graphite, LFP/Graphite, and NMC/LTO.
- evaluate the potential of hybrid battery configurations (NMC/Graphite,NMC/LTO) to mitigate degradation under increased cycling demand.

By quantifying degradation trends and trade-offs under representative operating scenarios, this research contributes to the development of battery systems and operational strategies that support the long-term and economically viable integration of electric vehicles into future energy systems.

To achieve these objectives, this thesis is organized as follows. Chapter 2 reviews the existing literature on lithium-ion battery degradation modeling, real-world operating conditions, and vehicle-to-grid (V2G) related aging, and identifies the research gaps addressed in this study. Chapter 3 provides technical background on lithium-ion battery technologies, including their operating principles, degradation mechanisms, and a comparative analysis of NMC/Graphite, LFP/Graphite ,and NMC/LTO chemistries from physical, degradation, and economic perspectives. Chapter 4 presents the development of the empirical degradation model for the NMC/LTO battery, including the adopted modeling methodology and the parameter identification procedure. Chapter 5 describes the simulation framework used in this study, integrating the degradation models with the vehicle model and constructing representative power profiles and simulation scenarios. Chapter 6 also presents and analyzes the simulation results, including cross-scenario comparisons and the economic evaluation of degradation costs. Finally, Chapter summarizes the main findings and contributions of the study, while Chapter 7 discusses the limitations of the work and provides recommendations for future research.

2

Literature Review

Lithium-ion battery degradation has been extensively studied due to its significant impact on battery lifetime and performance. Most existing research focuses on conventional lithium-ion chemistries such as NMC/Graphite and LFP/Graphite under controlled laboratory conditions. However, emerging chemistries such as lithium titanate oxide (LTO) and advanced operating modes such as Vehicle-to-Grid (V2G) introduce additional challenges for degradation analysis. This chapter reviews the existing literature on battery degradation modeling, real-world battery operation, and V2G-related aging and identifies the research gaps addressed in this study.

2.1. Limited Degradation Modeling for LTO

A wide range of battery degradation models has been proposed, including physics-based, empirical, semi-empirical, equivalent circuit, and data-driven approaches. Empirical and Semi-empirical models are widely used as they capture aging behavior using measurable parameters such as temperature, State of Charge (SoC), current rate, and cycling depth. Extensive modeling and experimental validation have been performed for common lithium-ion chemistries such as NMC/Graphite, NCA/Graphite, LFP/Graphite, and LCO/Graphite, resulting in a well-established understanding of their calendar and cycle aging behavior.For example, [3] delved into the calendar and cyclic aging of a Sanyo UR18650W NMC/Graphite cell, establishing a semi-empirical life model to account for both calendar-life and cycle-life losses. Similarly, [4] developed a semi-empirical model for both LFP/Graphite and NMC/Graphite chemistries. The model was then theoretically validated, with an average error of less than 4%. Furthermore, a simple semi-empirical life model was proposed for NCM622/graphite cells designed for high energy-density LIBs in [5], characterizing capacity fading according to a power law factor and Arrhenius kinetics.

In contrast, degradation modeling efforts for Lithium titanium Oxide (LTO)-based batteries remain limited. Existing studies on LTO batteries focus primarily on experimental characterization rather than the development of generalized degradation models. Experimental investigations such as those reported in [6] and [7] have provided valuable insight into the degradation behavior of NMC/LTO through extensive accelerated lifetime tests conducted under elevated temperatures, varying C-rates, and different cycle depths. These studies analyzed both capacity fade and internal resistance growth. In [6], a simplified lifetime model based on power-law fitting of capacity fade was proposed as a function of full equivalent cycles; however, this model was intended primarily for end-of-life estimation, resulting in limited accuracy during the early stages of aging and restricting its applicability. Similarly, [7] introduced a machine-learning-based model to estimate the state-of-health and predict the end-of-life. Although this approach achieved good predictive accuracy within the available data set, its limited physical interpretability restricts generalizability and complicates direct comparison with other lithium-ion battery chemistries. **This constitutes the first research gap: Lack of well-established empirical degradation models for LTO batteries comparable to those available for conventional lithium-ion chemistries**.

2.2. Battery Degradation under Realistic Driving and V2G Operations

Although numerous degradation models exist for common lithium-ion chemistries, as discussed in the previous section, most are developed and validated using standardized laboratory cycling tests. These tests typically rely on regular charge–discharge patterns and constant operating conditions, which fail to capture the complexity of real-world battery usage characterized by irregular load profiles, variable charging behavior, and intermittent rest periods. This limitation also applies to studies on Lithium Titanium Oxide (LTO)-based batteries, where degradation investigations are predominantly conducted under controlled laboratory conditions. As a result, the behavior of LTO batteries under realistic operating profiles remains insufficiently explored, and direct comparisons between LTO and conventional lithium-ion chemistries under real-world conditions are largely lacking.

Vehicle-to-Grid (V2G) operation introduces bidirectional power flow and additional cycles, which can significantly influence battery degradation. Several studies have investigated this effect for conventional lithium-ion batteries. [8]quantified the impact of V2G services on battery degradation using NMC/graphite-based batteries, demonstrating that increased energy throughput and deeper cycling accelerate capacity fading and reduce battery lifetime. A recent review [9] highlights that most V2G studies demonstrate accelerated cycle aging for conventional lithium-ion chemistries (e.g. NMC, LFP) and stresses the need for degradation modeling under realistic V2G conditions. However, these existing works are almost entirely limited to conventional lithium-ion chemistries such as NMC/graphite and LFP cells. The degradation behavior of lithium titanium oxide (LTO) batteries under V2G conditions remains largely unexplored, and, more importantly, there is a lack of comparative studies evaluating LTO against common lithium-ion chemistries under identical V2G usage. **This identifies the second research gap: Limited studies investigate battery degradation under realistic driving conditions and V2G operation while systematically comparing LTO batteries with conventional lithium-ion chemistries**.

2.3. Hybrid vs Conventional Battery Degradation under Driving and V2G Operations

Hybrid battery systems that combine different lithium-ion chemistries have been proposed as a promising approach to balance energy density, power capability, and battery lifetime in electric vehicles. For example, [10] investigated hybrid battery systems that combine LFP and LTO batteries to improve system performance and extend battery lifespan. The study shows that integrating LTO batteries to handle peak power demand can significantly reduce the stress on LFP batteries and extend their lifespan by more than 44% compared to a single-battery configuration. Similarly, [11] investigated a hybrid battery system composed of a high-energy NCA/graphite cell and a high-power LTO-based cell. The study analyzed cycle aging under realistic driving load profiles and demonstrated that shifting high-power demand to the LTO battery reduces stress on the high-energy battery and improves overall system lifetime. In addition, [12] investigated a hybrid energy storage system composed of high-energy NMC batteries and high-power LTO batteries. Their results show that hybridization allows the high-energy battery to supply continuous power while the high-power LTO battery handles short-term peak power demands, leading to reductions in system cost and weight compared to monotype battery systems.

Despite the promising results reported for hybrid battery architectures, most existing studies focus on specific hybrid configurations or operational strategies. Comparative analyzes between hybrid battery systems and conventional single-chemistry batteries in vehicle-to-grid (V2G) operation remain limited. Moreover, the long-term degradation behavior of hybrid lithium-ion battery configurations under both normal driving and V2G operating conditions has not been systematically investigated. Therefore, a comprehensive comparative assessment between hybrid battery systems and conventional lithium-ion chemistries under realistic driving and grid-interactive operating conditions is still lacking in the literature. **This highlights the third research gap: Lack of studies comparing hybrid lithium-ion battery systems with conventional battery chemistries under realistic driving and V2G conditions.**.

3

Lithium Ion Batteries

3.1. Lithium-Ion Battery

Since their initial commercialization in 1991, lithium-ion batteries (LIBs) have emerged as the leading electrochemical energy-storage technology. Their widespread adoption is primarily due to their high energy density, low self-discharge rate, superior round-trip efficiency, and extended cycle life[13]. Currently, Lithium-Ion Batteries are essential in diverse applications, including portable electronic devices, electric vehicles, and stationary energy storage systems that facilitate the integration of renewable energy.

3.1.1. Main Components

A typical lithium-ion battery (LIB) cell consists of four primary components as illustrated in 3.1:

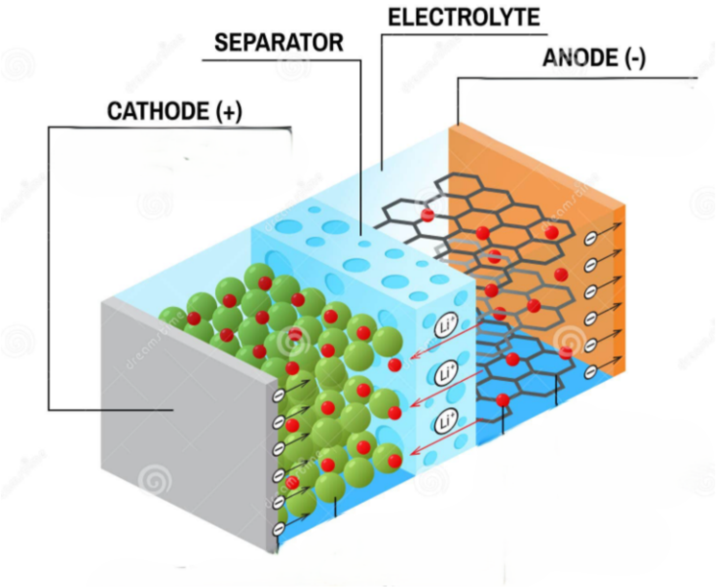

Figure 3.1: Components of a Lithium-Ion Battery [14]

Anode: The anode stores lithium ions during the charging process. Graphite is the most widely used anode material because of its stable layered structure, which enables efficient lithium intercalation. Alternative anode materials, such as silicon and lithium titanate (LTO), have been investigated to overcome the limitations of graphite; silicon offers a high theoretical specific capacity but experiences substantial volume expansion during cycling, while LTO provides enhanced safety and long cycle life.

Cathode: The cathode releases lithium ions during charging and hosts them during discharge. Common cathode materials include lithium cobalt oxide (LCO), lithium nickel manganese cobalt oxide (NMC), lithium nickel cobalt aluminum oxide (NCA), and lithium iron phosphate (LFP). The cathode composition plays a critical role in determining the nominal voltage, energy density, cost, and thermal stability of the cell.

Electrolyte: The electrolyte typically consists of a lithium salt (e.g., $LiPF_6$) dissolved in organic carbonate solvents. It must provide high ionic conductivity while remaining electronically insulating to prevent internal short circuits. The electrolyte composition also significantly influences the safety performance and the formation of solid electrolyte interphase (SEI) and cathode electrolyte interphase (CEI) layers.

Separator: A porous polymer membrane prevents electronic contact between the anode and cathode while allowing ionic transport.

3.1.2. Working Principle

The operation of a lithium ion battery is based on the reversible movement of lithium ions between the anode and the cathode through the electrolyte . This mechanism is illustrated in 3.2 where the arrows show the direction of ion flow.

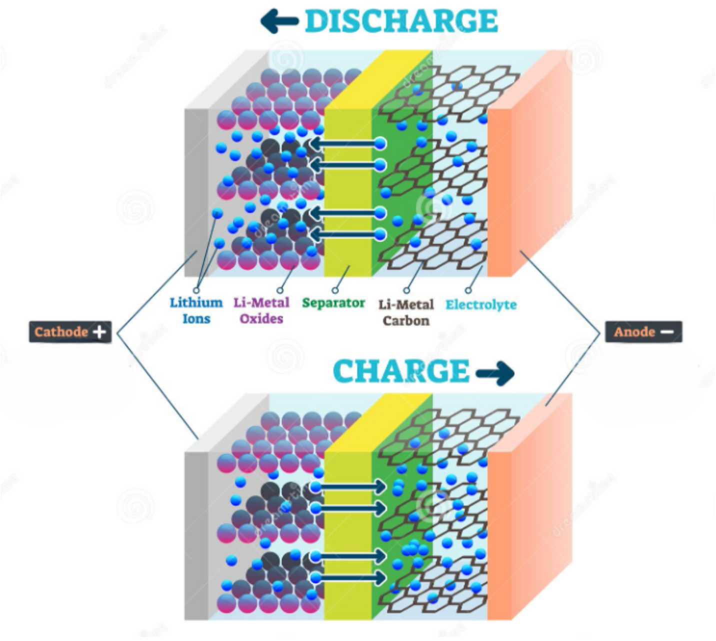

Figure 3.2: LIB During Charge and Discharge[14]

- **During Charging:** When an external power source applies a voltage, lithium ions are extracted (de-intercalated) from the cathode and travel through the electrolyte to the anode, where they are intercalated into the graphite layers. At the same time, electrons flow through the external circuit from the cathode to the anode, maintaining charge balance.
- **During discharge:** The process is reversed. Lithium ions move from the anode back to the cathode, and electrons flow through the external circuit to provide electrical power to the connected device.

3.1.3. Key Characteristics

Key advantages of LIBs include:

- High gravimetric energy density (commonly up to $\sim 250\,\mathrm{Wh/kg}$);
- High round-trip efficiency (>90%);
- Low self-discharge and absence of memory effect;
- Long cycle and calendar life under appropriate operating conditions.

Despite this success, challenges remain regarding cost, safety, and especially degradation(the gradual loss of capacity with time and use). Therefore, understanding how different cell chemistries behave and degrade is crucial to improving battery life.

3.2. Lithium-Ion Battery Chemistries

The electrochemical characteristics of a lithium-ion cell are determined primarily by the combination of its cathode and anode materials. Each electrode material contributes distinct attributes that influence overall performance, including energy density, power density, thermal stability, cost, and cycle life.

3.2.1. Cathode Chemistries

- **Lithium Cobalt Oxide (LCO)**: exhibits a relatively high nominal voltage (3.7 V) and a specific capacity in the range of 140–160 $\mathrm{mAh\,g^{-1}}$). These characteristics enable a high energy density and stable cycling performance, which explains its widespread use in portable electronic devices. However, LCO suffers from limited thermal stability and high material cost due to cobalt content.
  Applications: Portable electronics such as smartphones and laptops [15].
- **Lithium Iron Phosphate ($LiFePO_4$, LFP)**: LFP offers excellent thermal and chemical stability, outstanding safety, and a long cycle life. However, its lower operating voltage (~3.2 V) and moderate energy density make it less suitable for high-energy applications.
  Applications: Electric busses, stationary energy storage and power tools [15].
- **Lithium Nickel Manganese Cobalt Oxide ($LiNi_xMn_y\ Co_{1-x-y}O_2$, NMC)**: NMC materials balance energy density, power capability and cost, with tunable compositions (e.g., NMC111, NMC532, NMC811). Increasing the nickel content enhances capacity but reduces thermal stability.
  Applications: Electric vehicles and hybrid energy systems [15].

- **Lithium Nickel Cobalt Aluminum Oxide ($LiNi_{0.8}Co_{0.15}Al_{0.05}O_2$, NCA)**: NCA offers high specific energy and long cycle life, but exhibits moderate thermal stability and higher material cost.
  Applications: High-performance electric vehicles and aerospace systems [15].
- **Lithium Manganese Oxide ($LiMn_2O_4$, LMO)**: The spinel-structured LMO features low cost, good rate performance and improved safety. However, it suffers from limited cycle life due to manganese dissolution and structural degradation at elevated temperatures.
  Applications: Power tools and short-range EVsc̃itenitta2015li.

3.2.2. Anode Chemistries

- **Graphite (C_6)**: The dominant commercial anode due to its low cost, good electrical conductivity, and stable formation of the solid electrolyte interphase (SEI). Its theoretical capacity is 372 mAh g^{-1}, with a low operating potential (~0.1 V vs. Li^+/Li). However, it is prone to lithium plating during high-rate charging. *Applications:* All current commercial LIBs.[15][16].
- **Silicon-Based (Si, Si-C Composites)**: Silicon offers a much higher theoretical capacity (3,600 mAh/g) , far exceeding graphite. However, large volume expansion (~300%) during cycling causes mechanical degradation and unstable SEI formation. Composite anodes that combine silicon with graphite or carbon are in development. *Applications:* High-energy electric vehicles (EV) and next-generation LIBs [15][17].
- **Tin- and Antimony Based alloying materials (Sn, Sb, and Alloys)**: These alloying materials provide capacities higher than those of graphite but experience significant volume-change-induced degradation, limiting practical application. *Applications:* Research and niche cells [15][17].
- **Metal Oxide and Composite Anodes (e.g., TiO_2, Nb_2O_5)**: Transition-metal oxides provide improved rate capability and thermal stability, but their energy density remains moderate. *Applications:* Solid-state and hybrid lithium-ion systems [15].
- **Lithium Titanate ($Li_4Ti_5O_{12}$, LTO)**: LTO is a “zero-strain” spinel anode material known for its outstanding structural stability, long cycle life, and exceptional safety. Table 3.1compares the electrochemical and structural characteristics of lithium titanate (LTO) and graphite anodes.

Table 3.1: Comparison of selected anode properties for LTO vs. Graphite.

Property	**LTO ($Li_4Ti_5O_{12}$)**	**Graphite (C_6)**
Working potential (V vs. Li/Li^+)	1.55	0.10
Volume change (%)	~0.2	~12
Lithium diffusion coefficient (cm^2/s)	10^{-8} to 10^{-12}	10^{-10} to 10^{-14}
SEI formation	Negligible	Forms during first charge

As shown in the table, LTO exhibits a very small volume change during lithiation (0.2%) compared to graphite (12%), which contributes to its excellent structural stability and long cycle life. In addition, LTO has a significantly higher lithium diffusion coefficient than graphite, enabling faster lithium transport and supporting high power capability and rapid charging. Its relatively high operating potential (~1.5 V vs. Li^+/Li) effectively suppresses the formation of the solid electrolyte interphase (SEI) and eliminates lithium plating, which commonly degrades graphite-based anodes. This property enables excellent cycle and calendar life as well as superior thermal stability. However, the higher anode potential reduces the overall cell voltage and energy density compared to graphite-based systems. Consequently, LTO is favored in applications that prioritize safety, power capability, and fast charging over energy density, such as grid-scale storage and electric busses [15] [18]

3.3. Lithium-Ion Battery Degradation

Battery degradation refers to the gradual reduction in the capacity and power output of a cell over time.

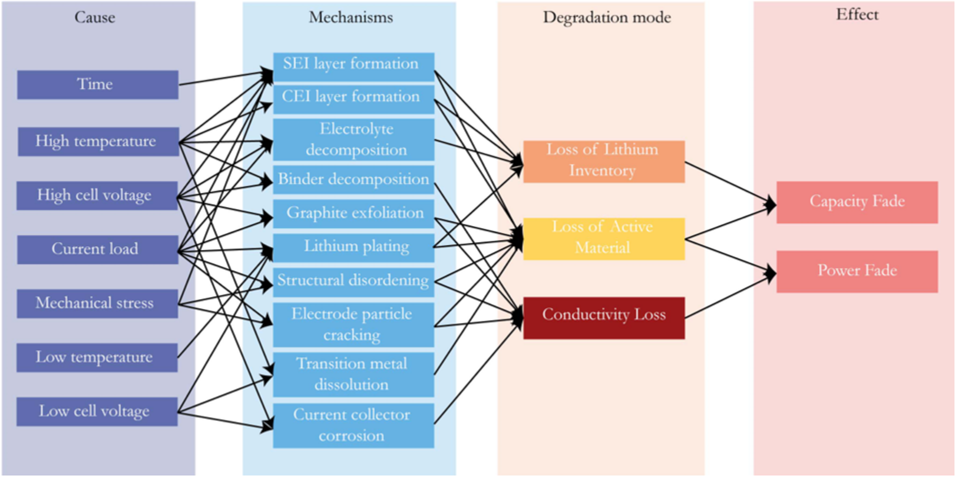

Figure 3.3: Overview of the correlation between stress factors, aging mechanisms, aging mode, and their effect on LIB [13]

Figure 3.3 illustrates the relationship between the causes, mechanisms, degradation modes, and resulting effects observed in lithium-ion batteries (LIBs).

3.3.1. Degradation Modes

LIB aging is categorized into three different modes [13]

1. **Loss of Lithium Inventory (LLI):** Irreversible side reactions consume cyclable lithium, reducing the available capacity.
2. **Loss of Active Material (LAM):** Mechanical or structural changes reduce accessible intercalation sites.
3. **Conductivity Loss (CL):** Increased internal resistance from, e.g., current-collector corrosion or binder degradation.

The relative contribution of these modes depends on operating conditions such as temperature, state of charge (SoC), current rate, and cell chemistry.

3.3.2. Degradation Mechanisms

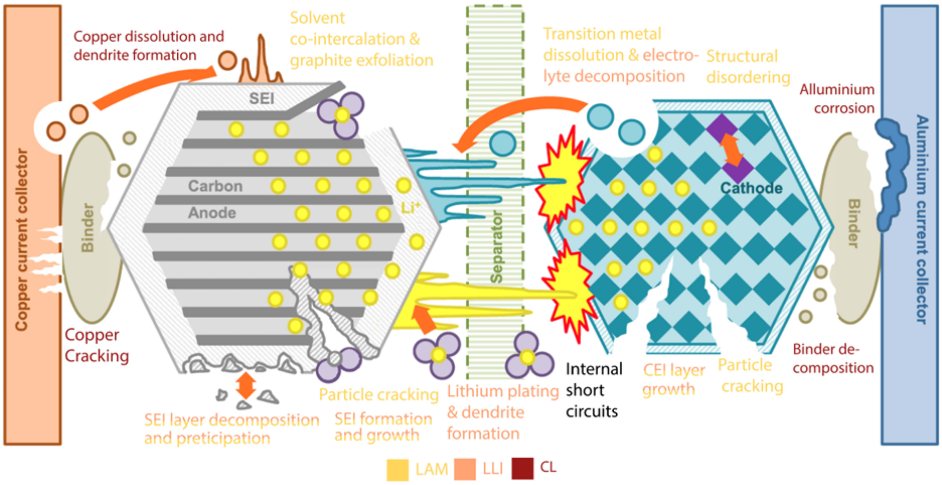

Figure 3.4: Aging mechanisms occurring within lithium-ion batteries (LIBs) [13]

Figure 3.4 provides a graphical representation of the major aging mechanisms occurring within lithium-ion batteries (LIBs). The illustration distinguishes between the degradation processes that take place at the anode and the cathode.

Anode Aging Mechanisms

At the anode, multiple coupled physicochemical processes drive performance degradation and safety risks in lithium-ion batteries. The most common mechanisms are summarized below.

- **Solid Electrolyte Interphase (SEI) Formation:** Graphite anodes operate at very low voltages (0.05 to 1 V vs. Li/Li^+), which are outside the electrochemical stability window of common organic electrolytes. This results in a reduction in electrolytes and the formation of a solid electrolyte interphase (SEI) layer—a thin passivation film that protects the anode but consumes cyclable lithium. Initially, SEI formation stabilizes the electrode surface; however, continued reactions and cracking during cycling lead to further SEI growth, causing additional loss of lithium and increased impedance.
  The rate of SEI formation is strongly influenced by temperature, the state of charge (SoC), and storage time. Higher temperatures and higher SoC accelerate SEI growth, and layer thickness typically increases with the square root of time ($\propto \sqrt{t}$), consistent with diffusion-controlled kinetics [19] [13] [20].

- **Lithium Plating:** At low temperatures or during high charging rates, the anode potential can fall below 0 V versus Li/Li^+, causing metallic lithium to deposit on the anode surface instead of intercalating in the graphite structure. This phenomenon leads to permanent capacity loss and represents a significant safety hazard due to the formation of lithium dendrites that may penetrate the separator and induce internal short circuits. Lithium plating is a self-reinforcing process—once initiated, it accelerates further degradation and often produces distinct “knee points” in the cell’s capacity-fade trajectory [19] [20] [13].

- **Mechanical Stress and Particle Cracking:** During cycling, lithium intercalation and deintercalation cause periodic volume changes in the graphite anode. These volume fluctuations generate mechanical stress, which can lead to particle cracking and loss of electrical contact between the active material particles and the conductive matrix. Such microstructural damage results in the loss of active material (LAM) and an additional loss of lithium inventory (LLI) through repeated reformation of SEI [20] [13].

- **Transition Metal Deposition:** Transition metals (e.g. Ni, Mn, and Co) that dissolve from the cathode during cycling can migrate through the electrolyte and deposit on the anode surface. These metallic deposits act as catalysts for parasitic side reactions, accelerating SEI growth and promoting lithium plating. This cross-electrode contamination contributes significantly to long-term performance decline [19] [13].
- **Alternative Anode Materials:**
  - **Lithium Titanate ($Li_4Ti_5O_{12}$, LTO):** Operates at a higher potential ($\sim$1.5 V vs. Li/Li^+), effectively preventing SEI formation and lithium plating. LTO anodes offer superior cycle life, power capability and safety, but exhibit lower energy density due to reduced cell voltage [15] [18].
  - **Silicon (Si):** It has an exceptionally high theoretical capacity (~3580 mAh g^{-1}), but it undergoes extreme volumetric expansion (~280%) during cycling. This repeated expansion and contraction cause severe mechanical degradation and rapid capacity fading [15][17].

Cathode Aging Mechanisms

At the cathode, degradation arises mainly from interfacial film formation, structural transformations, and transition-metal dissolution. These processes reduce the availability of lithium and alter the electronic and ionic transport pathways.

- **Cathode Electrolyte Interphase (CEI):** At high positive potentials, electrolyte oxidation produces a surface film—commonly referred to as the cathode electrolyte interphase (CEI). Although partially protective, this layer increases the interfacial impedance and can trigger gas evolution and electrolyte decomposition under elevated voltage or temperature conditions [19] [20].
- **Structural Changes:** Layered oxide cathodes, such as NMC and NCA, undergo phase transitions, lattice distortion, and oxygen loss during cycling. Manganese-rich spinel systems (e.g., $LiMn_2O_4$) are particularly prone to Jahn–Teller distortion, which induces lattice expansion and mechanical stress, leading to micro-cracking and progressive loss of active material[19].
- **Transition-Metal Dissolution:** Transition metals (Ni, Co, Mn) can dissolve from the cathode into the electrolyte, especially under high-voltage or high-temperature operation. This dissolution not only depletes the lithium inventory within the cathode but also promotes parasitic reactions when redeposited at the anode. The resulting cross-electrode degradation contributes to impedance growth, capacity fade, and, in severe cases, internal short circuits [19].

.

3.3.3. Ageing

Calendar Ageing

Calendar aging refers to the loss of capacity during storage or idle operation.

- **Time:** The capacity fade increases with time even at rest, as the SEI continues to thicken. Over long periods, small parasitic reactions also consume electrolyte and lithium [13].
- **Temperature:** Reaction rates increase with temperature (Arrhenius behavior). Roughly, SEI growth rates can double for each increase 10 °C. Above 60 °C, electrolyte decomposition can trigger thermal repulsion. LFP and LTO tend to be more heat-tolerant; NMC/NCA degrade faster at elevated temperatures [13] [19]
- **State Of Charge (SOC):** Higher SoC levels correspond to higher electrode potentials, which enhance electrolyte oxidation and SEI formation. Capacity fade is generally faster when cells are stored near 100% SoC compared to 50% or less [13].

Cyclic Ageing

Cyclic aging results from repeated charge-discharge cycles and the mechanical and electrochemical stresses they impose.

- **Throughput:** Throughput (the total charge cycled through the battery) directly correlates with capacity loss. Higher throughput increases electrode fatigue, particle cracking, and SEI reformation [13] [21].
- **Temperature:** The heat generated during cycling accelerates chemical degradation and inhomogeneous reaction rates. NMC/NCA often degrades significantly above 45 °C, whereas LFP performs best below 35 °C [13] [19].
- **Mean SoC and Depth of Discharge (DoD):** Deeper DoD leads to larger volume changes in graphite, causing microcracks and additional SEI formation. NMC and NCA show a stronger dependence on DoD than LFP. For batteries with LTO anode, this dependency is minimal because of its zero-strain nature [19] [21].
- **Current Rate:**

  Higher C-rates accelerate degradation due to increased overpotential and heat generation. However, for some NCA cells, faster cycling at moderate C-rates can reduce overall calendar aging since the time at high SoC is shortened [13].

3.4. Modelling of Battery Degradation

Battery degradation modeling approaches differ in complexity, precision, and data requirements. Table 3.2 compares the main modeling techniques used for the analysis of lithium-ion battery aging.

Table 3.2: Comparison of Battery Degradation Modelling Techniques [13]

Model Type	Complexity	Accuracy	Data Requirement
Physics-Based Models (PBM)	High	High	Low–Medium
Equivalent Circuit Models (ECM)	Medium	Medium	Medium–High
Machine Learning Models (MLM)	Medium–High	Medium–High	High
Empirical / Semi-Empirical Models (EM)	Low	Low–Medium	Medium–High

Physics-based models achieve high accuracy by explicitly capturing electrochemical degradation mechanisms, but they are computationally intensive and mainly suited for battery and material design studies. Equivalent circuit models offer a balance between simplicity and accuracy, making them attractive for real-time applications such as battery management systems and online state-of-health estimation. Machine learning models rely on large datasets to predict degradation behavior and are effective for data-driven diagnostics, though they lack physical interpretability. Empirical and semi-empirical models are computationally efficient and well suited for long-term system-level simulations, lifetime estimation, and optimization studies; however, their accuracy is limited to the operating conditions used for model calibration.

3.5. Comparison Across Chemistries

This section compares the lithium-ion battery chemistries considered in this study, namely nickel–manganese-cobalt (NMC), lithium iron phosphate (LFP), and lithium titanate oxide (NMC-LTO) batteries. The comparison is limited to these chemistries, as they form the basis of the degradation models and hybrid configurations investigated later in this work. The comparison is structured into three aspects: physical and chemical characteristics, degradation behavior, and cost and environmental considerations.

3.5.1. Physical and Chemical Characteristics

The physical and chemical properties of the battery chemistries determine their energy capability, power performance, safety, and thermal behavior. Table 3.3 summarizes the key characteristics of batteries based on NMC and LFP.In addition, LTO as anode material.

Table 3.3: Physical and chemical comparison of battery chemistries [21] [22] [15] [23] [18]

Property	**NMC-Graphite**	**LFP-Graphite**	**NMC-LTO**
Nominal Voltage (V)	3.6	3.2	2.26
Energy Density ($\mathrm{Wh\,kg^{-1}}$)	165	120	74
Power Density ($\mathrm{W\,kg^{-1}}$)	~ 600–800	~ 1,000–2,000	~3,000–7,000
Operating Temperature Range (°C)	~ −20 to 55	~ −20 to 60	~ −30 to 60
Thermal Stability	Moderate	High	Very High
Safety	Moderate	High	Very High

NMC batteries offer high energy density, making them attractive for electric vehicle applications, but they exhibit moderate thermal stability and safety characteristics. LFP batteries provide lower energy density but improved thermal stability and intrinsic safety. LTO-based batteries, while having significantly lower energy density as a result of their higher anode potential, exhibit exceptionally high power capability, wide operating temperature range, and superior safety characteristics, which make them suitable for high power and grid-interactive applications.

3.5.2. Degradation Characteristics

Battery degradation is strongly influenced by operating conditions such as temperature, depth of discharge, state of charge, and charge–discharge rates. Table 3.4 qualitatively compares the degradation sensitivity of the considered chemistries.

Table 3.4: Qualitative comparison of degradation characteristics [24] [18] [21] [22] [15] [23]

Degradation Factor	**NMC-Graphite**	**LFP-Graphite**	**NMC-LTO**
Sensitivity to High Temperature	High	Medium	Low
Sensitivity to High SoC	High	Medium	Low
Sensitivity to High DoD Cycling	Medium–High	Medium	Low
Sensitivity to High C-rates	Medium	Medium	Very Low
Calendar Aging	Medium	Low	Very Low
Cycle Aging	Medium–High	Medium	Low

NMC batteries are particularly sensitive to high temperatures and high states of charge, which can accelerate both calendar and cycle aging. LFP batteries exhibit improved degradation resistance because of their stable olivine structure, which leads to reduced sensitivity to temperature and state-of-charge effects. LTO-based batteries demonstrate the lowest degradation sensitivity across all considered factors, primarily due to the absence of solid electrolyte interphase growth on the anode and their high tolerance to fast charge–discharge cycling. These characteristics make LTO-based systems particularly attractive for Vehicle-to-Grid operation.

3.5.3. Cost and Environmental

Cost and environmental considerations are critical for the large-scale deployment of battery technologies in electric vehicles and grid-interactive applications. Table 3.5 summarizes typical cost ranges and key environmental aspects of the battery chemistries considered in this study.

Table 3.5: Cost and environmental comparison of battery chemistries [25] [26] [27] [28]

Property	**NMC-Graphite**	**LFP-Graphite**	**NMC-LTO**
Pack Cost (USD kWh^{-1})	65	50	200
Critical Materials	Ni, Co	Fe, P	Ti
Cobalt Content	High	None	None
Environmental Risk	Medium–High	Low	Low
Recyclability	Moderate	High	High
Expected Cycle Life (Cycles)	1,000–2,000	2,000–4,000	>10,000

NMC batteries exhibit moderate pack-level costs but rely on critical materials such as nickel and cobalt, which introduce supply-chain volatility and environmental concerns. LFP batteries benefit from lower cost and the absence of cobalt, leading to improved environmental performance and high recyclability. LTO-based batteries present the highest upfront cost, mainly due to their lower energy density and manufacturing complexity; however, their extremely long cycle life and enhanced safety characteristics can significantly reduce the total cost of ownership, particularly in applications involving frequent cycling such as Vehicle-to-Grid operation.

4

(NMC/LTO) Degradation Model

This chapter presents the methodology used to develop the degradation model for the NMC/LTO battery. First, the reference papers used in this study are introduced. The procedure for extracting the experimental data is described, followed by the adoption of a power-law formulation to represent the degradation behavior. Subsequently, the model fitting process is presented. Finally, the obtained model is introduced, followed by its validation.

4.1. Modeling Methodology

The degradation model developed in this study is based on the findings reported in papers [7]and [6], both of which employed identical experimental setups and testing conditions for high-power lithium titanate oxide (LTO) cells. Consequently, these studies provide consistent and comparable experimental results that describe the behavior of capacity fade across varying cycle depths, current rates, and operating temperatures.

The experimental data sets used for the construction of the model in this work are taken from the paper [7], which presents detailed measurements of capacity loss under a wide range of operating conditions. However, the data were not available in numerical form. Therefore, they were extracted from the published figures through data digitization.

The modeling approach adopted in this work follows the power law degradation formulation proposed in [6], where the same experimental data set was analyzed to characterize battery capacity fade. After digitizing the experimental data, the MATLAB Curve Fitting Tool was used to estimate the parameters of the adopted power law degradation model. To ensure an accurate representation of the degradation behavior, a sequence of four fitting procedures was performed, leading to the identification of the final degradation model.

4.2. Data Extraction

The experimental data required for model development were not available directly in numerical form; therefore, the data set used in this study was extracted from published figures reported in [7]. Data digitization was performed to reconstruct the capacity fade behavior of the investigated lithium titanate oxide (LTO) cells under different operating conditions.

A data set describing capacity fade as a function of full equivalent cycles (FEC) was first obtained by digitizing a figure that illustrates capacity evolution at a fixed cycle depth of 50% and a temperature of 42.5 °C for multiple charge-discharge rates. A similar procedure was applied to another figure that presents capacity degradation at a constant charge–discharge rate of 2C and the same temperature for various cycle depths. It should be noted that the experimental data extracted were from cycling tests. Therefore, the reported capacity degradation includes calendar aging that accumulates simultaneously during cycling. As a result, the developed aging model will not represent purely cyclic degradation; rather, it reflects the combined effects of cycle-induced degradation and concurrent time-dependent aging processes during experimental cycling tests.

4.3. Power-Law Relationship for Battery Degradation

In this study, a power-law degradation model is adopted due to limitations in the available experimental data, which were accessible only through the digitization of published figures, as discussed previously. This process yielded a sparse and noisy dataset. Although polynomial fitting can provide acceptable performance when modeling the influence of a single stress factor, extending the approach to account for multiple stress factors led to poor generalization, pronounced overfitting, and non-physical surface curvature. In contrast, the power-law formulation yields a smooth degradation that aligns well with experimentally observed aging behavior. Furthermore, the model parameters offer clear physical interpretability and naturally capture the multiplicative interaction of key stress factors such as cycle depth and current rate. For these reasons, data limitations, robustness against overfitting, physical interpretability, and improved predictive performance, the power-law approach is selected as the basis for the LTO degradation modeling.

As illustrated in Figure 4.1, the referenced study identifies three regions of capacity degradation . These regions correspond to different aging regimes governed by different dominant physical mechanisms.

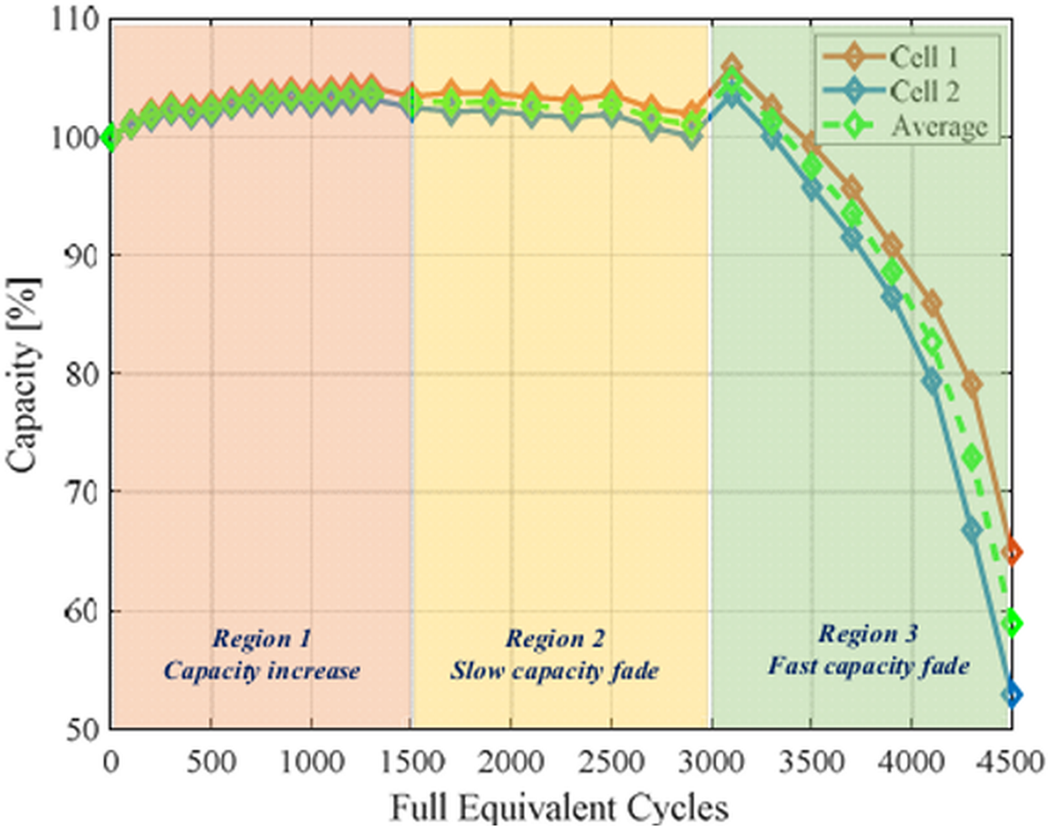

Figure 4.1: The three regions of capacity degradation in LTO batteries [6].

- **Region I – Capacity Increase (Activation Phase)**

  The slight increase in capacity, a behavior that has been widely reported for lithium titanate oxide (LTO) batteries and other lithium ion chemistries [7] [6] [29] [30].
  This phenomenon is commonly attributed to the increased electrode active surface area as a result of electrochemical milling, which happens due to the redistribution of lithium ions between layers, as well as stabilization of chemical reactions [31]. That means that during repeated lithiation and delithiation, lithium ions are inserted into and extracted from the host material, generating small but continuous local strains within the electrode particles. In earlier cycles, these strains can cause slight particle rearrangements, surface renewal, or exposure of previously inaccessible reaction sites. Consequently, a larger portion of the active material becomes electrochemically accessible, leading to improved lithium-ion transport and enhanced charge-transfer kinetics. Furthermore, early cycling promotes the stabilization of chemical and interfacial reactions. Initial parasitic reactions, such as the formation of the solid electrolyte interphase (SEI) at the anode or the cathode electrolyte interphase (CEI), gradually evolve into more stable and passivating layers.

- **Region II – Slow Capacity Fade (Stable Aging Phase)**

  In this region, the capacity fade proceeds slowly and approximately linearly with cycling. The degradation is mainly governed by a gradual loss of cyclable lithium and steady growth of the interfacial layers, such as the solid–electrolyte interphase (SEI), as well as mild structural changes within the electrodes. Mechanical and electrochemical stresses are largely balanced, resulting in predictable and limited capacity degradation.

- **Region III – Fast Capacity Fade (Accelerated Aging Phase)**

  Beyond a critical point often referred to as “aging knee” capacity loss accelerates significantly. This phase is marked by the onset of more severe degradation mechanisms, including pronounced particle cracking, electrode delamination, loss of electronic connectivity, and bulk structural damage. Once started, these mechanisms lead to a rapid increase in internal resistance and irreversible loss of active material, resulting in strongly nonlinear capacity fade behavior.

The adopted formulation follows the methodology presented in [6], in which the capacity fading of lithium titanate oxide (LTO) batteries is described using an empirical power-law function. The general mathematical form is as follows:

$$\mathbf{C_{fade}} = x \cdot FEC^{y}$$

Where:

- C_{fade}, the percentage of capacity loss relative to the beginning of life (BOL),
- FEC, the number of full equivalent cycles,
- x and y , empirical coefficients that describe the degradation rate and its dependence on cycling conditions.

Physical Interpretation of Empirical Coefficients

The empirical coefficients x and y influence the degradation of the battery in a different way in the three aging regions .

1. **Region I**
    - The slight increase in capacity observed during the early cycle is neglected and degradation is assumed to be almost zero. This assumption is made because the power-law formulation is not suited to represent the reversible capacity changes.
2. **Region II**
    - Both coefficients x and y contribute to the degradation behavior. However, x largely determines the baseline rate of capacity loss, resulting in an approximately linear degradation.
3. **Region III**
    - The exponent y dominates the degradation behavior, introducing a strong nonlinearity and pronounced curvature in the fading trajectory of the capacity as the degradation accelerates.

In summary, the coefficient x governs the initiation of degradation and sets the initial scale of capacity loss, while the exponent y controls the acceleration of degradation with continued cycling. In particular, y determines the slope of the degradation curve and can be interpreted as an indicator of the dominant aging mechanisms that act in later stages of battery life. By expressing x and y as functions of operating stress factors, such as cycle depth and current rate, the proposed power-law formulation provides a physically meaningful and computationally efficient framework for predicting capacity fade.

4.4. Model Fitting

The digitized experimental data were fitted using the MATLAB Curve Fitting Tool to estimate the parameters of the adopted power-law degradation model. Initially, the model parameters were identified as functions of the cycle depth only. In a subsequent stage, the influence of the current rate was incorporated through an additional fitting procedure. However, it was observed that introducing the current rate affected the parameters previously identified as cycle-depth-dependent. Consequently, an additional refitting stage was required to recalibrate the cycle-depth-related parameters while accounting for the current rate. A similar interdependence was also observed for the parameters associated with the current rate. This observation motivated a final fitting stage in which both sets of parameters were determined simultaneously to ensure consistency within the model.

This iterative fitting procedure allowed the final model parameters to capture the coupled influence of both cycle depth and current rate on battery degradation. The results of the fitting process are presented and discussed progressively throughout this section. At each stage, the adequacy of the formulation obtained is evaluated to determine whether further refinement is required.

4.4.1. Initial Fitting

In the initial stage, experimental data corresponding to a current rate of $C_r = 2$ and cycle depths of 10%, 30% and 50% were fitted to derive a surface that describes the loss of capacity as a function of cycle depth and full equivalent cycles:

$$C_{\text{fade}} = x(cd) \cdot FEC^{y(cd)} \tag{4.1}$$

The resulting fitted surface, along with the experimental measurements, is shown in Figure 4.2.

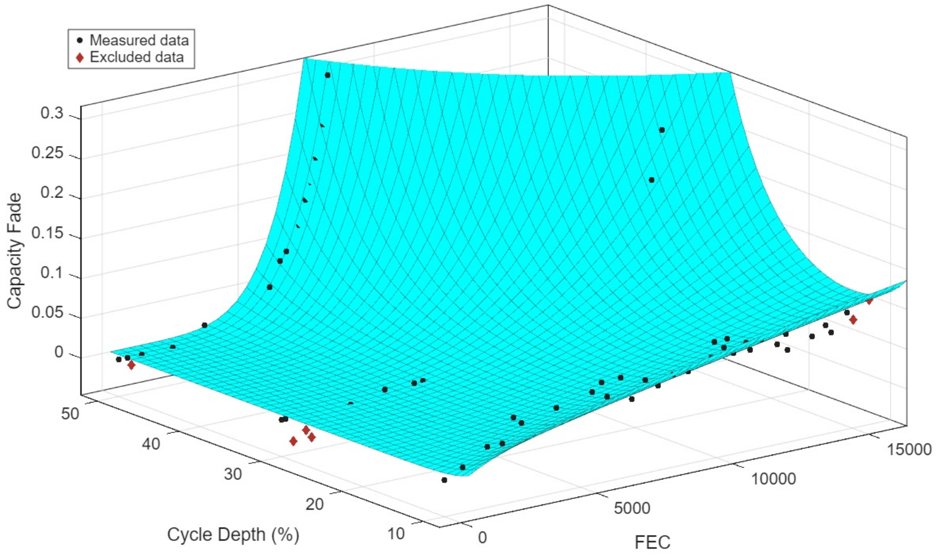

Figure 4.2: Capacity fade as a function of full equivalent cycles (FEC) and cycle depth (cd), showing experimental data and the fitted model surface.

The fitting procedure resulted in

$$C_{\text{fade}} = 0.999 \cdot e^{-1.029\,cd} \cdot FEC^{(0.055\,cd^{1.182})} \tag{4.2}$$

The goodness-of-fit metrics for the proposed model are summarized in Table 4.1.

Table 4.1: Goodness-of-fit metrics for the Initial fitting .

Metric	**Value**
R^2	0.9376
SSE	0.0183
RMSE	0.0162

The high coefficient of determination (R^2 = 0.9376) indicates that the model explains approximately 94% of the observed variability in capacity degradation. Furthermore, the low values of the sum of squared errors (SSE = 0.0183) and the root mean square error (RMSE = 0.0162) confirm that the fitting errors are small, demonstrating good agreement between the experimental data and the fitted surface. Figure 4.3 compares the capacity fade predicted by Equation 4.2 with the experimental data as a function of full equivalent cycles.

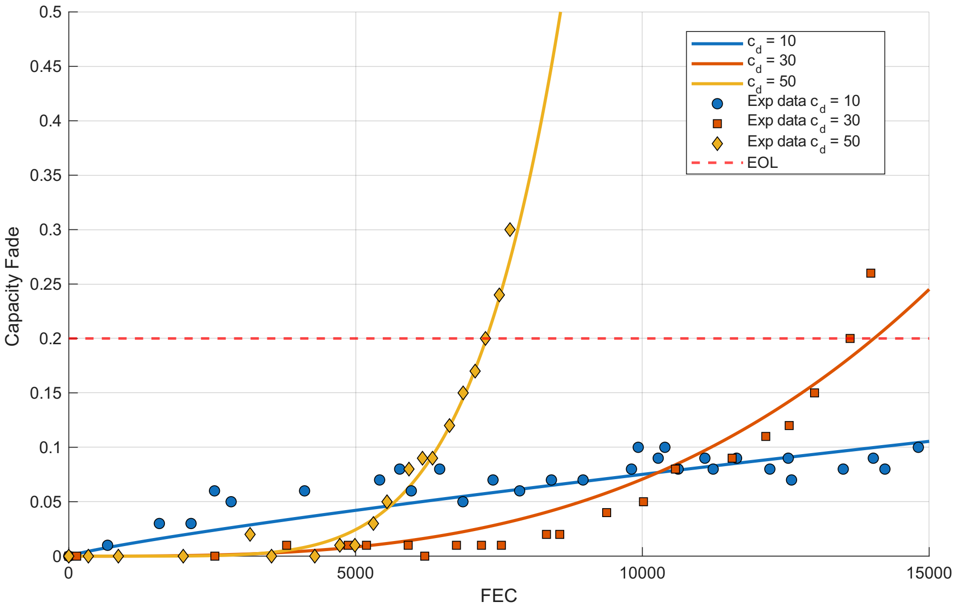

Figure 4.3: Capacity fade as a function of full equivalent cycles (FEC) for cycle depths of 10%, 30%, and 50% at $C_r = 2$.

The model fits the experimental data well for the selected current rate and cycle depths, as indicated by the high coefficient of determination and low error values. However, it is limited to a single current rate and cannot describe degradation under different charge–discharge rates. To overcome this limitation, the effect of the current rate is included in the next modeling step.

4.4.2. Incorporating the Effect of Current Rate

Based on the capacity fade model defined in Equation 4.2, the influence of the current rate (c_r) was incorporated to extend the model. Consequently, the model was reformulated as follows

$$C_{\text{fade}} = x(cd, c_r) \cdot FEC^{y(cd, c_r)} \tag{4.3}$$

Separable dependencies between the cycle depth and the current rate were assumed. Consequently, the model was reformulated as follows.

$$C_{\text{fade}} = 0.999 \cdot e^{-(1.029\,cd + a\,c_r)} \cdot FEC^{\left(0.055\,cd^{1.182} \cdot b\,c_r^{d}\right)} \tag{4.4}$$

where a, b, and d are fitting parameters that capture the influence of the current rate. The fitted surface obtained from experimental data at multiple current rates and a fixed cycle depth of 50% is illustrated in Figure 4.4.

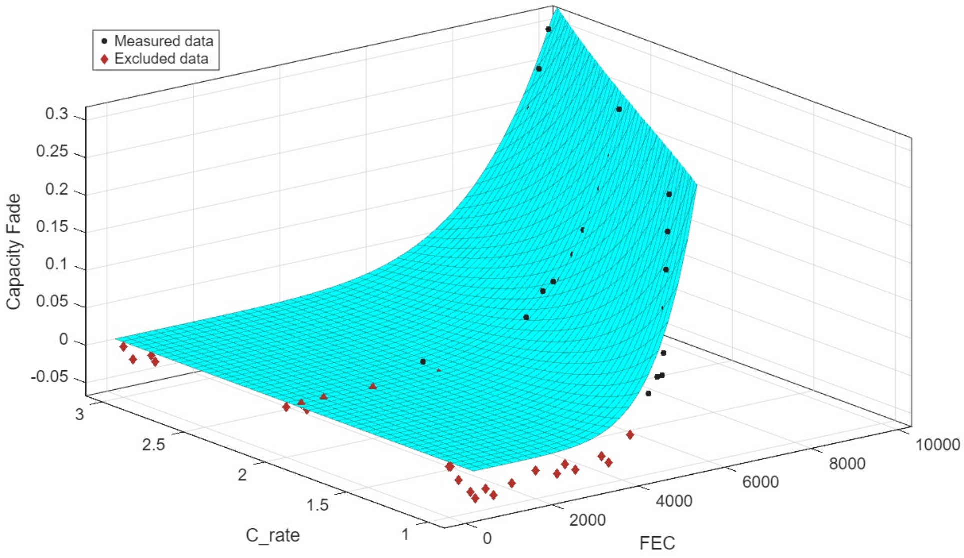

Figure 4.4: Capacity fade as a function of full equivalent cycles (FEC) and current rate (c_r), showing experimental data and the fitted model surface at $cd = 50\%$.

The resulting fitted model is given by

$$C_{\text{fade}} = 0.999 \cdot e^{-(1.029\,cd+0.84\,c_r)} \cdot FEC^{\left(0.055\,cd^{1.182} \cdot 1.057\,c_r^{-0.031}\right)} \tag{4.5}$$

Table 4.2 summarizes the goodness-of-fit statistics for the proposed model.

Table 4.2: Goodness-of-fit metrics for teh second fitting .

Metric	**Value**
R^2	0.8103
SSE	0.0470
RMSE	0.0417

The coefficient of determination ($R^2 = 0.8103$) indicates that approximately 81% of the variability in capacity fade is captured by the model. Although the fitting accuracy is lower than that achieved in the case of single-current rates, the SSE (0.0470) and RMSE (0.0417) values remain within an acceptable range, indicating reasonable agreement between the experimental data and the fitted surface.

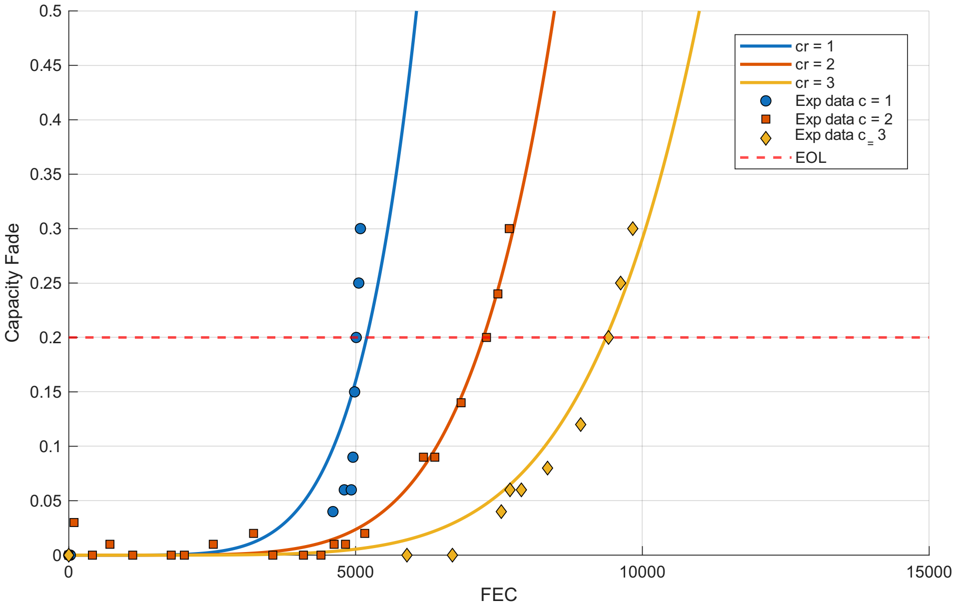

Figure 4.5: Capacity fade as a function of full equivalent cycles (FEC) for cd = 50% at different current rates.

Figure 4.5 presents a comparison between the predicted and experimental capacity fade as a function of the full equivalent cycles at a fixed cycle depth of 50% for different current rates. The close agreement observed indicates that the proposed model provides a satisfactory fit to the experimental data. However, this level of agreement is not observed when comparing model predictions across different cycle depths at a fixed current rate of $C_r = 2$. As shown in Figure 4.6.

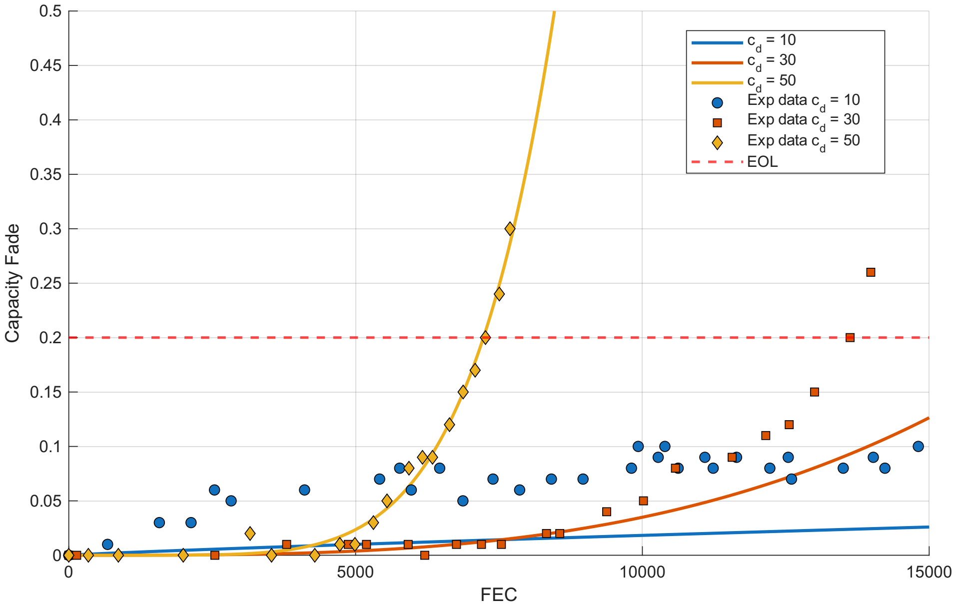

Figure 4.6: Capacity fade as a function of full equivalent cycles (FEC) for cycle depths of 10%, 30%, and 50% at $C_r = 2$.

The extended model accurately represents the experimental data at a cycle depth of 50%, while reduced accuracy is observed at cycle depths of 10% and 30%. This discrepancy occurs because the model parameters were calibrated using data collected at a fixed cycle depth of 50% at different current rates. Therefore, recalibrating the model with data covering a wider range of both cycle depths is necessary to improve its predictive performance.

4.4.3. Refining the Model for Cycle Depth Dependence

To address the reduced predictive accuracy observed at different cycle depths in the last step, the experimental datasets corresponding to multiple cycle depths were re-fitted to update the cycle depth-dependent parameters $x(cd)$ and $y(cd)$. The revised generalized expression for capacity fade was formulated as

$$C_{\text{fade}} = 0.999 \cdot e^{-(a\,cd+0.84\,c_r)} \cdot FEC^{\left(b\,cd^{d} \cdot 1.057\,c_r^{-0.031}\right)} \tag{4.6}$$

The fitted surface obtained from the combined data set is shown in Figure 4.7, illustrating the relationship between capacity fade, full equivalent cycles, and cycle depth.

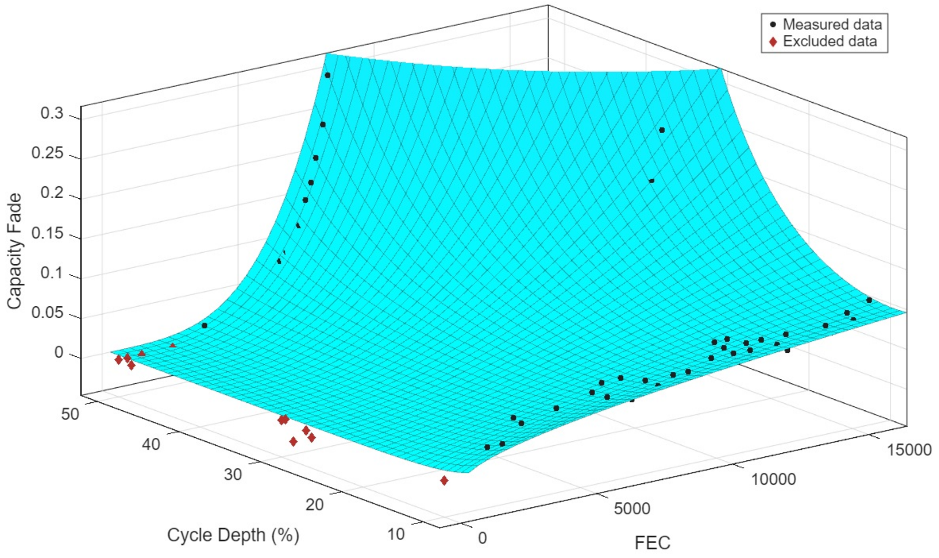

Figure 4.7: Capacity fade as a function of full equivalent cycles (FEC) and cycle depth (cd), showing experimental data and the fitted model surface.

The resulting fitted model is expressed as

$$C_{\text{fade}} = 0.999 \cdot e^{-(0.648\,cd+0.84\,c_r)} \cdot FEC^{\left(0.044\,cd^{1.120} \cdot 1.057\,c_r^{-0.031}\right)} \tag{4.7}$$

Table 4.3 summarizes the goodness-of-fit metrics for the refined model.

Table 4.3: Goodness-of-fit metrics for the thrid fitting

Metric	**Value**
R^2	0.7692
SSE	0.0542
RMSE	0.0298

The goodness-of-fit results indicate that the model captures the overall degradation trend with reasonable accuracy. The coefficient of determination ($R^2 = 0.7692$) suggests that approximately 77% of the variability in the loss of capacity is explained by the model. The corresponding values of SSE (0.0542) and RMSE (0.0298) indicate moderate fitting errors, reflecting acceptable agreement between different cycle depths and current rates. Figure 4.8 compares the model predictions with experimental data for different cycle depths at a fixed current rate of $C_r = 2$.

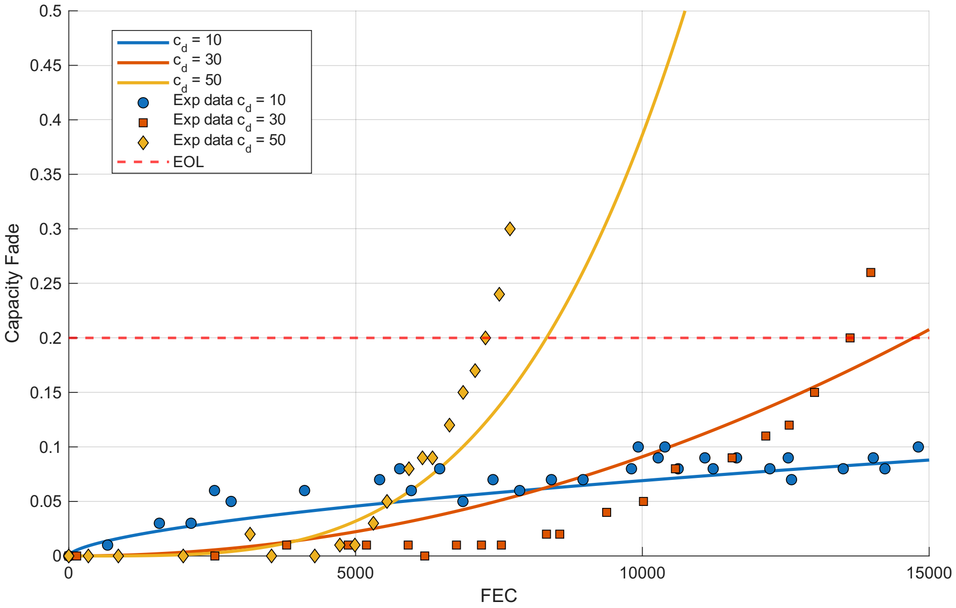

Figure 4.8: Capacity fade as a function of full equivalent cycles (FEC) for cycle depths of 10%, 30%, and 50% at $C_r = 2$.

The refined model provides an accurate fit at a cycle depth of 10%. However, noticeable discrepancies are observed for cycle depths of 30% and 50%, particularly at higher values of full equivalent cycles.

A similar trend is observed when the model is evaluated at a fixed cycle depth of 50% across varying current rates, as illustrated in Figure. 4.9. Although the model performs well at lower current rates, a reduced accuracy is observed at higher current rates, particularly for the largest cycle depth.

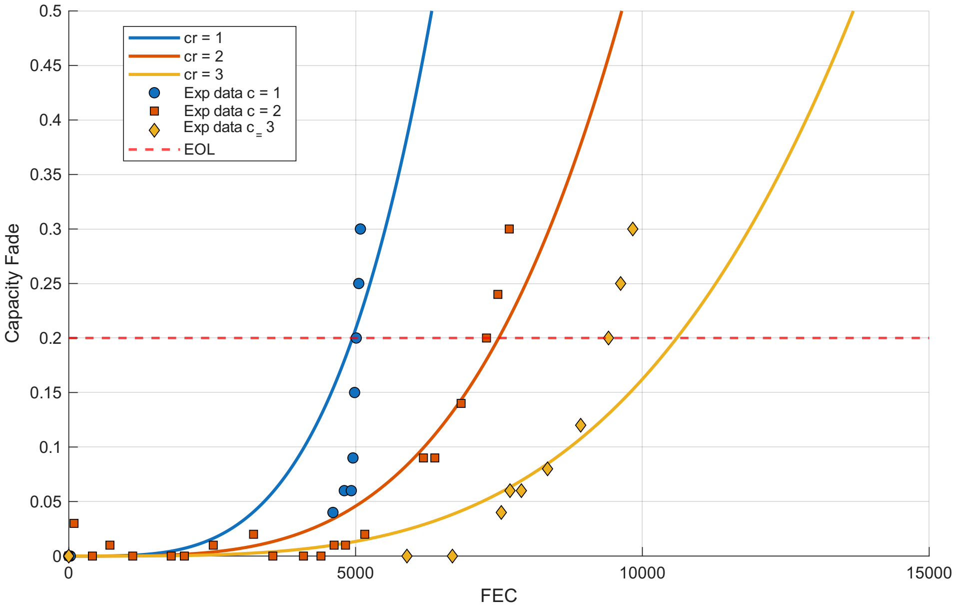

Figure 4.9: Capacity fade as a function of full equivalent cycles (FEC) at $cd = 50\%$ for different current rates.

When the effects of cycle depth and current rate were combined, the parameters associated with both stress factors changed compared to when each was fitted independently. This indicates an interaction between cycle depth and current rate in their influence on degradation behavior. As a result, a subsequent adjustment step was required to recalibrate the model parameters simultaneously, ensuring that the final model accurately reflects the coupled impact of both operating conditions.

4.4.4. Final fitting

To obtain a more general and robust degradation model, datasets corresponding to various current rates were re-fitted using Equation 4.7. In this final step, both the depth of the cycle (cd) and the current rate (c_r) were treated as coupled stress factors that influence the depletion of the capacity. The generalized formulation is expressed as follows.

$$C_{\text{fade}} = 0.999 \cdot e^{-(0.648\,cd + a\,c_r)} \cdot FEC^{\left(0.044\,cd^{1.120} \cdot b\,c_r^{d}\right)} \tag{4.8}$$

where a, b, and d are fitting parameters associated with the current rate dependence. The fitted surface obtained from this formulation is shown in Figure 4.10.

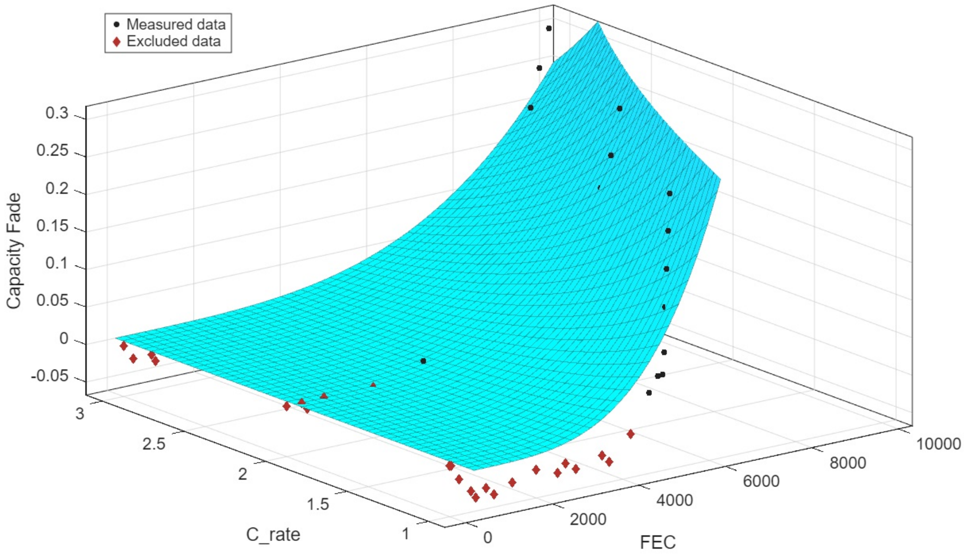

Figure 4.10: Capacity fade as a function of full equivalent cycles (FEC) and current rate (c_r), showing experimental data and the fitted model surface.

The final empirical relationship derived from the fitting procedure is given by

$$C_{\text{fade}} = 0.999 \cdot e^{-(0.648\, cd + 0.918\, c_r)} \cdot FEC^{\left(0.044\, cd^{1.120} \cdot 1.049\, c_r^{-0.007}\right)}. \tag{4.9}$$

Table 4.4 summarizes the goodness-of-fit metrics obtained under fixed cycle depth conditions.

Table 4.4: Goodness-of-fit metrics for the final capacity fade model

Metric	Value
R^2	0.70
SSE	0.0761
RMSE	0.0531

The goodness-of-fit results indicate a reduction in predictive accuracy compared to the previous model formulations. The coefficient of determination ($R^2 \approx 0.70$) suggests that approximately 70% of the observed variability in capacity fade is captured by the model. The relatively higher values of the sum of squared errors (SSE) and the root mean square error (RMSE) reflect an increased uncertainty in the fitting process when both stress factors are incorporated simultaneously.

As observed throughout the sequential fitting stages, the predictive accuracy of the model decreased as additional variables were incorporated. This reduction in accuracy can be attributed to the combined influence of cycle depth (cd), and current rate (cr) on battery degradation. Accurately capturing the coupled effects of these variables generally requires a large and comprehensive experimental dataset covering a wide range of operating conditions. However, as discussed previously, such datasets are scarce, which constrains the parameter identification process. Despite these limitations, the final fitting stage yielded a coefficient of determination of $R^2 = 0.7$, which can be considered acceptable for an empirical degradation model based on limited experimental data. Therefore, the resulting Equation 4.9 can be regarded as a suitable approximation for describing capacity fade as a function of full equivalent cycles (FEC), cycle depth (cd), and current rate (cr),and provides a physically meaningful representation of the degradation behavior depending on these factors. The validity of the model will be evaluated in the following section.

4.5. Final model and validation

The final empirical relationship derived from the fitting procedure is given by

$$\boxed{C_{\text{fade}} = 0.999\, e^{-(0.648\, cd + 0.918\, c_r)}\, FEC^{(0.044\, cd^{1.120} \cdot 1.049\, c_r^{-0.007})}} \tag{4.10}$$

where :

- C_{fade}: normalized capacity fade
- FEC: full equivalent cycles
- cd : cycle depth (10,30,50,...)
- c_r : current rate (1,2,3,...)

From the coefficients of Equation 4.10, it can be observed that cycle depth (cd) appears in both the exponential term and the power-law exponent with comparatively larger coefficients. This indicates that cycle depth has a dominant influence on the degradation behavior and represents the most influential operating condition affecting battery capacity fade.

To assess the validity of the developed model, its predictions were compared with the experimental data by plotting both results together. Furthermore, additional cycle depth (cd) conditions were examined to evaluate how well the model captures the influence of this key degradation factor.

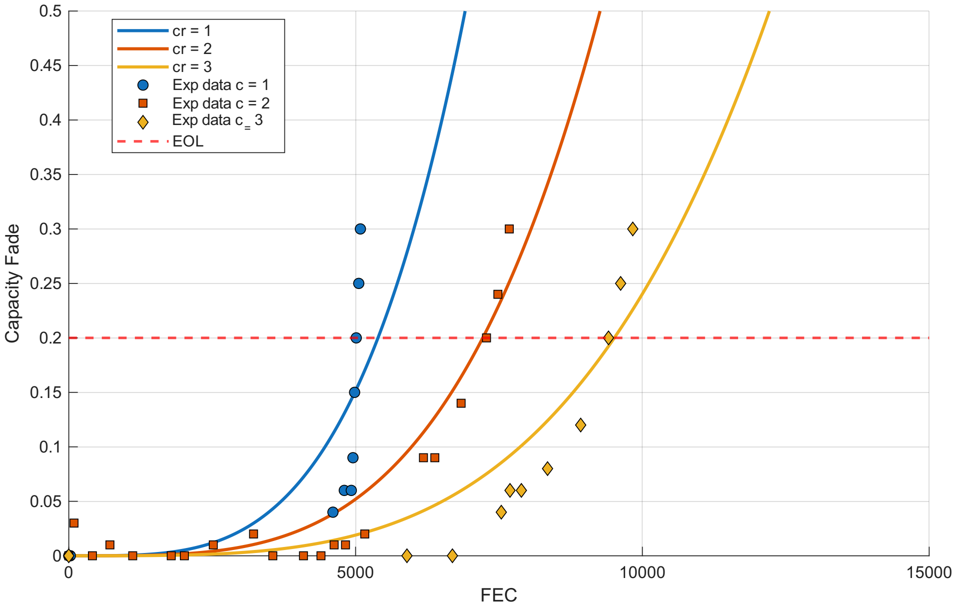

Figure 4.11: Capacity fade as a function of full equivalent cycles (FEC) at $cd = 50\%$ for different current rates.

Figure 4.11 compares the model predictions with experimental data at a fixed cycle depth of 50% and varying current rates. As shown, the model accurately reproduces the experimental trends for $c_r = 2$ and $c_r = 3$. Reduced accuracy is observed at $c_r = 1$, which can be attributed to the limited availability of experimental data under this condition. Importantly, the model performs well during the early FECs, which is the most relevant region for the subsequent analysis presented in this study. In addition, the predicted end-of-life (EOL) point closely matches the experimental observations. Furthermore, the model reveals an interesting trend of decreasing capacity fade with increasing current rate, a behavior that has also been observed in both reference studies.

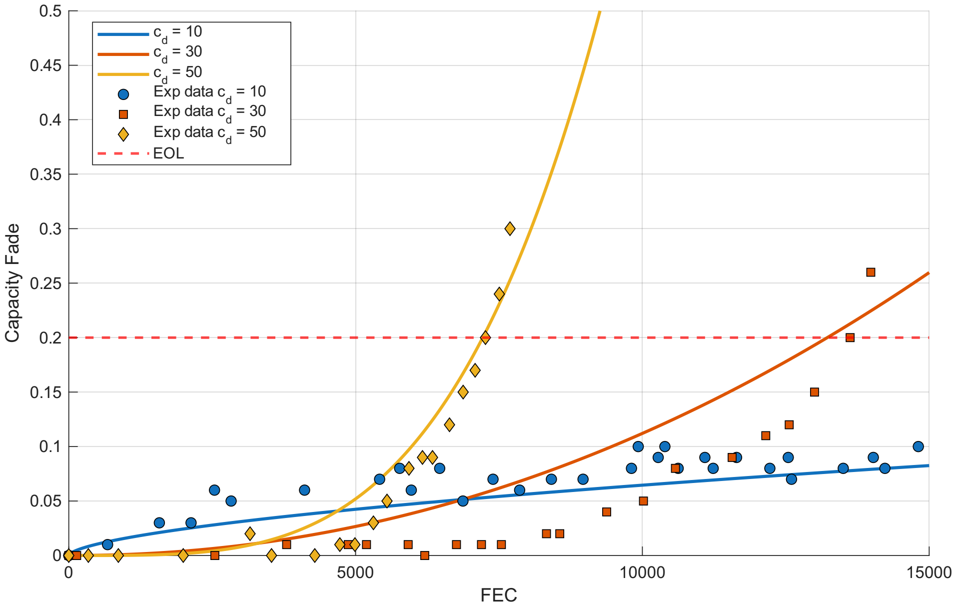

Figure 4.12: Capacity fade as a function of full equivalent cycles (FEC) for cycle depths of 10%, 30%, and 50% at $C_r = 2$.

Figure 4.12 presents the comparison at a fixed current rate of $C_r = 2$ at different cycle depths. The model accurately captures the degradation behavior at cycle depths of 10% and 50%, while deviations are observed at 30% cycle depth, particularly at higher FEC values. Nevertheless, good agreement is achieved in the early degradation region and near the EOL point. The model also correctly predicts the overall trend of increasing capacity fade with increasing cycle depth. This trend is further illustrated in Figure 4.13, which highlights the dominant influence of cycle depth on degradation behavior.

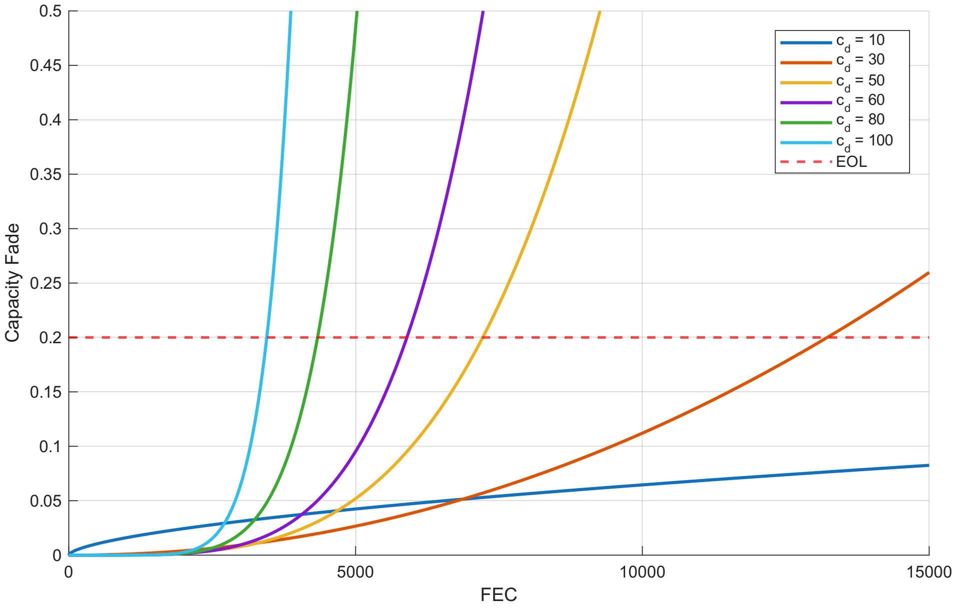

Figure 4.13: Capacity fade trends as a function of cycle depth .

As shown , increasing cycle depth significantly accelerates capacity fade and leads to an earlier onset of the knee point, thereby reducing the overall battery lifetime. However, in the initial region, where degradation remains low and is approximately linear, the shallow cycling $cd = 10\%$ exhibits a comparatively higher apparent degradation than the deeper cycling. This behavior becomes more evident in Figure 4.14, where the model predictions are shown over the first 200 FEC.

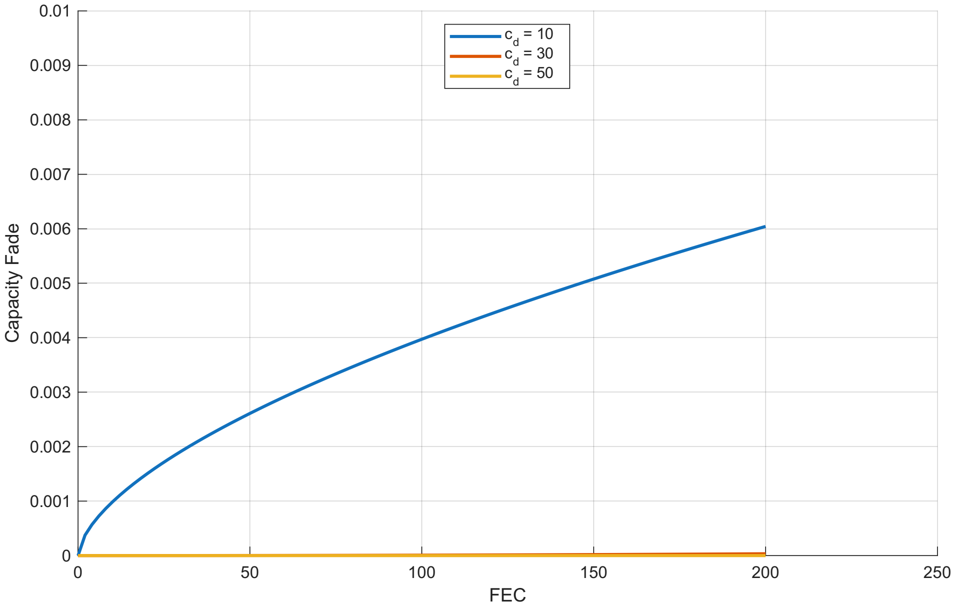

Figure 4.14: Predicted capacity fade over the first 200 full equivalent cycles for different cycle depths.

In this early-life region, cycle depths of 30% and 50% exhibit lower apparent capacity fade compared to 10%. This behavior is attributed to early-cycle phenomena (Activation Phase), increased electrode active surface area 4.3, which are more pronounced at higher cycle depths and are modeled here as near-zero degradation.

Overall, the model captures the degradation behavior by reflecting the increase in capacity fade with higher cycle depth and the decrease in degradation with higher current rates. The model was also validated against experimental data for different cycle depths and shows good agreement. However, the level of agreement for different current rates is comparatively lower.

5

Simulation

This chapter describes the two-year simulation framework used to evaluate battery performance. It adopts degradation models for two common chemistries, namely NMC/Graphite and LFP/Graphite, in addition to the NMC/LTO degradation model developed in Chapter 4. A hybrid battery configuration combining NMC/Graphite and NMC/LTO cells is also proposed. The chapter then presents the vehicle model and the applied power profiles under both normal driving and vehicle-to-grid (V2G) operations. Subsequently, three simulation scenarios are introduced, followed by the presentation and discussion of the results for each scenario and a comparison between them. Finally, an economic assessment of the obtained results is conducted.

5.1. Degradation Models

The cyclic aging models employed in this thesis incorporate the calendar aging component that accumulates simultaneously during cycling operation. Model 1 and Model 2, are adopted from the comparative implementation and analysis presented by [32]. Model 3 corresponds to the degradation model developed within the scope of this study and is described in detail in Chapter 4. Finally, Model 4 represents a hybrid configuration that combines Model 1 and Model 3.

5.1.1. Model 1 (Cyclic Aging Model for NMC Cells)

Model 1 [21] was originally developed for NMC-based lithium-ion cells and describes both cyclic and calendar aging. The pure cyclic aging behavior is expressed as

$$\boxed{C_{\text{cyclic}} = 1 - \beta\sqrt{\text{throughput}}} \tag{5.1}$$

$$\beta = 7.348 \times 10^{-3}(\bar{V} - 3.667)^2 + 7.600 \times 10^{-4} + 4.081 \times 10^{-3}\Delta DoD \tag{5.2}$$

Where :

- $\bar{V}$: mean cell voltage during a cycle
- ΔDoD: depth of discharge for a cycle
- throughput (Ah): cell throughput

The calendar again is given as

$$\boxed{C_{\text{calendar}} = 1 - \alpha\, t^{0.75}} \tag{5.3}$$

$$\alpha = (7.543 \times V - 23.75) \times 10^{6} \times e^{-\frac{6976}{T}} \tag{5.4}$$

Where :

- V: cell voltage
- T: temperature (K)
- t: time (days)

Equation 5.1 is used to determine the pure cyclic aging. Subsequently,Equation 5.3 is applied to incorporate calendar aging that occurs simultaneously during cycling. In this formulation,t represents the cumulative cycle time, and T denotes the operating temperature during the cycling period.

5.1.2. Model 2 (Cyclic Aging Model for LFP Cells)

Model 2 [22] was developed for lithium-ion cells based on lithium iron phosphate (LFP) and describes cyclic and calendar aging. The cyclic aging model consists of two components. The first describes the high-temperature contribution and captures the temperature dependence of cyclic aging, while the second represents the low-temperature contribution and accounts for the C-rate dependence. The total cyclic aging is obtained by summing these two contributions.

$$\boxed{Q_{L,\text{cyc}} = Q_{L,\text{cyc,highT}} + Q_{L,\text{cyc,lowT}}} \tag{5.5}$$

$$Q_{L,\text{cyc,highT}} = k_{\text{cyc,highT}}(T)\sqrt{Q_{\text{tot}}} \tag{5.6}$$

$$Q_{L,\text{cyc,lowT}} = k_{\text{cyc,lowT}}(T, I_{\text{ch}})\sqrt{Q_{\text{ch}}} \tag{5.7}$$

$$k_{\text{cyc,highT}}(T) = k_{\text{cyc,highT,ref}} \exp\left[-\frac{E_{a,\text{cyc,highT}}}{R}\left(\frac{1}{T} - \frac{1}{T_{\text{ref}}}\right)\right] \tag{5.8}$$

$$k_{\text{cyc,lowT}}(T) = k_{\text{cyc,lowT,ref}} \exp\left[\frac{E_{a,\text{cyc,lowT}}}{R}\left(\frac{1}{T} - \frac{1}{T_{\text{ref}}}\right)\right] \exp\left[\beta_{\text{lowT}} \frac{I_{\text{ch}} - I_{\text{ch,ref}}}{C_0}\right] \tag{5.9}$$

Where :

- Q_{tot}: total cell throughput (Ah)
- Q_{ch}: charging cell throughput (Ah)
- $E_{a,\text{cyc,highT}}$: activation energy for cyclic ageing at high temperature

- $E_{a,\mathrm{cyc,lowT}}$: activation energy for cyclic ageing at low temperature
- R: universal gas constant (8.314 J mol^{-1}K^{-1})
- T: temperature (K)
- T_{ref}: reference temperature (298.15 K)
- I_{ch}: charging current (A)
- $I_{\mathrm{ch,ref}}$: reference charging current
- C_0: nominal cell capacity
- β_{lowT}: empirical model constant

The calendar aging component is described as

$$\boxed{Q_{L,\mathrm{cal}}(t) = k_{\mathrm{cal}}(T, \mathrm{SoC}) \cdot \sqrt{t}} \tag{5.10}$$

$$k_{cal}(T, SoC) = k_{cal,ref} \exp\left[-\frac{E_{a,cal}}{R}\left(\frac{1}{T} - \frac{1}{T_{ref}}\right)\right]\left(\exp\left[\frac{\alpha F}{R}\left(\frac{U_{a,ref} - U_a(SoC)}{T_{ref}}\right)\right] + k_0\right) \tag{5.11}$$

Where :

- $E_{a,\mathrm{cal}}$: activation energy for calendar ageing
- R: universal gas constant (8.314 J mol^{-1}K^{-1})
- T: temperature (K)
- T_{ref}: reference temperature (298.15 K)
- F: Faraday constant
- $U_{a,\mathrm{ref}}$: reference half-cell potential
- U_a: half-cell potential of the anode
- α, k_0: equation constants
- t: time (hours)

The cyclic aging equation 5.5 was used to determine the pure cyclic degradation component. Subsequently, the calendar aging term 5.10 is added to account for the degradation accumulated simultaneously during cycling. In this formulation,t represents the cumulative duration of cycling, and T denotes the operating temperature during the cycling process.

5.1.3. Model 3 (Cyclic Aging Model for LTO Cells)

The degradation behavior of lithium titanate oxide batteries (NMC/LTO) is evaluated using the empirical degradation model that developed and validated in 4.5. The model describes capacity fade as a function of full equivalent cycles (FEC), cycle depth (cd), and current rate (c_r), thus capturing the dominant cycling-related stress factors influencing the aging of LTO. The final degradation model is expressed as

$$\boxed{C_{\text{fade}} = 0.999 \cdot e^{-(0.648\,cd + 0.918\,c_r)} \cdot FEC^{(0.044\,cd^{1.120} \cdot 1.049\,c_r^{-0.007})}} \tag{5.12}$$

Where :

- C_{fade}: normalized capacity fade
- FEC: full equivalent cycles
- cd: cycle depth
- c_r: current rate

This power-law-based formulation incorporates the coupled effects of the cycle depth and current rate through physically interpretable parameters. The model has been shown to accurately capture the early and mid-life degradation behavior of LTO batteries and to provide reasonable predictions of end-of-life capacity trends within the validated operating range.

5.1.4. Model 4 (Hybrid Model (Model 1 + Model 3))

Model 4 represents a hybrid battery degradation framework that combines the cyclic aging behavior of **NMC/Gr cells**, modeled using **Model 1**, and **NMC/LTO cells**, modeled using **Model 3**. The primary objective of this hybrid approach is to exploit the advantages of the two chemistries. While NMC batteries offer high gravimetric energy density and relatively low cost, LTO batteries provide superior cycling stability and high power capability. By integrating both chemistries within a single battery pack, the hybrid model aims to mitigate the overall capacity loss while maintaining an acceptable system-level cost and mass.

In practical applications, the fraction of LTO cells in hybrid battery systems is constrained by economic and weight-related considerations. Compared to NMC batteries, LTO cells exhibit a substantially higher cost per kilowatt-hour and a significantly lower gravimetric energy density,as presented in Table 5.1.

Table 5.1: Comparison of cost and gravimetric energy density for NMC and LTO battery chemistries 3.5 3.3

Battery Chemistry	Cost (USD/kWh)	Gravimetric Energy Density (Wh/kg)
NMC (Nickel Manganese Cobalt)	~65	~165
LTO (Lithium Titanate Oxide)	~200	~74

Due to these characteristics, increasing the proportion of LTO cells results in a pronounced increase in overall system cost as well as a higher battery mass for a given energy capacity. Therefore, these limitations restrict the feasible integration of LTO cells to relatively small fractions within hybrid battery architectures. Accordingly, two hybrid model configurations are considered:

- **Model 4-a:** 90% NMC (Model 1) + 10% LTO (Model 3)
- **Model 4-b:** 85% NMC (Model 1) + 15% LTO (Model 3)

The difference between the two configurations corresponds to a modest increase of 5% in the LTO share. This range was deliberately selected to represent a practical design modification at the system-level rather than an extreme hybridization scenario. The comparison between Model 4-a and Model 4-b enables a sensitivity analysis of how incremental increases in LTO content affect capacity fade over time, highlighting the trade-off between improved cycling durability and increased cost and mass.

In this hybrid configuration, a sequential utilization strategy is adopted. During discharge, the NMC/LTO supplies the power demand first due to its superior cycling stability, after which the NMC/Graphite battery provides the remaining energy. The same strategy is applied during charging, where the NMC/LTO is charged first, followed by the NMC/Graphite battery.

5.2. Vehicle Model and Parameters

In this study, the **BMW i3 (120 Ah)** electric car vehicle was adopted, whose key specifications are summarized in Table 5.2.

Table 5.2: BMW i3 parameters .

Parameter	**Value**
Vehicle mass (unladen)	1345 kg
Drag coefficient (C_d)	0.29
Frontal area (A_f)	2.38 m^2
Rolling resistance coefficient (C_{rr})	0.015
Battery pack voltage	352 V
Battery capacity	42.2 kWh (120 Ah)
Cell configuration	96 S 1 P
Drivetrain efficiency (η_{drive})	0.95

5.3. Power profile

In this study, two battery power profiles are used, both derived from the **World Harmonized Light-Duty Vehicle Test Procedure (WLTP)** drive cycle for Class 3 vehicles, which are characterized by a power-to-weight ratio greater than 34 W/kg. The WLTP driving cycle represents realistic urban, suburban, rural, and highway driving conditions and includes frequent acceleration, deceleration, and regenerative braking events, making it suitable for degradation analysis under real-world operation.

The methodology used to generate the first battery power profile (Power Profile 1) is adopted from the work presented in [32]. This approach is subsequently extended in this study to construct a second battery power profile (Power Profile 2).Battery power is obtained as follows:

$$P = F_t \cdot v$$

Where F_t the drag force and v is the instantaneous velocity of the vehicle.

WLTP velocity profile was converted into a power profile by computing the tractive force (F_t) acting on the vehicle at each time step. This force results from:

- *Aerodynamic drag* ($F_d = 0.5\rho C_d A_f v^2$),
- *Rolling resistance* ($F_{rr} = f_r mg$),
- *Acceleration or deceleration* ($F_a = m\frac{dv}{dt}$).

The total tractive force was then used to calculate instantaneous battery power. where positive power represents discharge and negative power corresponds to regenerative braking (assumed 70% efficient).

5.3.1. Power Profile 1 (Driving and Charging)

To represent daily operation, two WLTP driving cycles and one charging event were combined to construct a day-long power profile representing an A→B→A commute, followed by vehicle charging using a home charger with a rated power of 7.4 kW. Figures 5.1 and 5.2 illustrate the resulting daily battery power demand and state-of-charge (SOC) profiles.

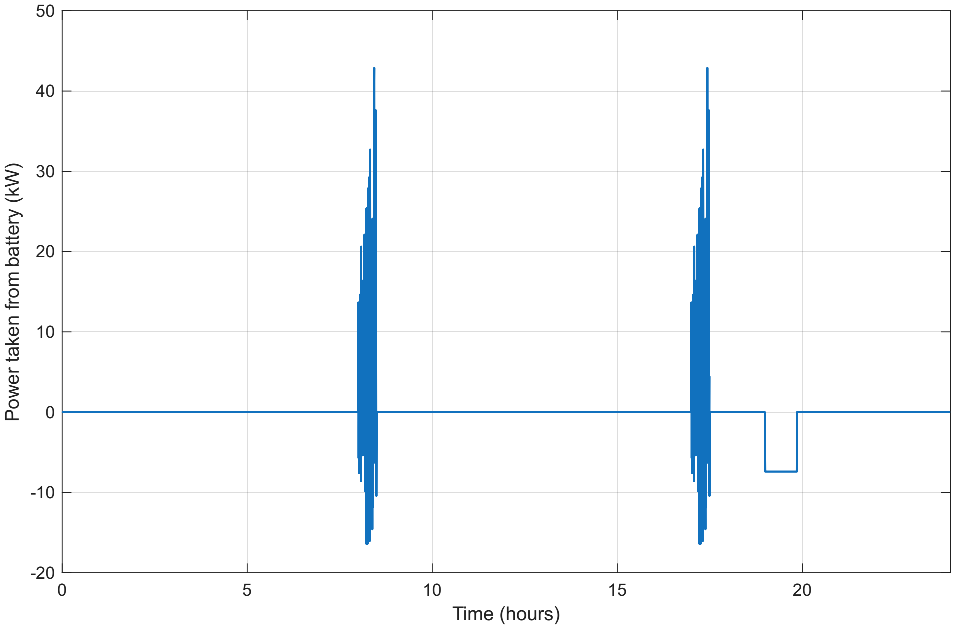

Figure 5.1: Power profile 1 for a full day

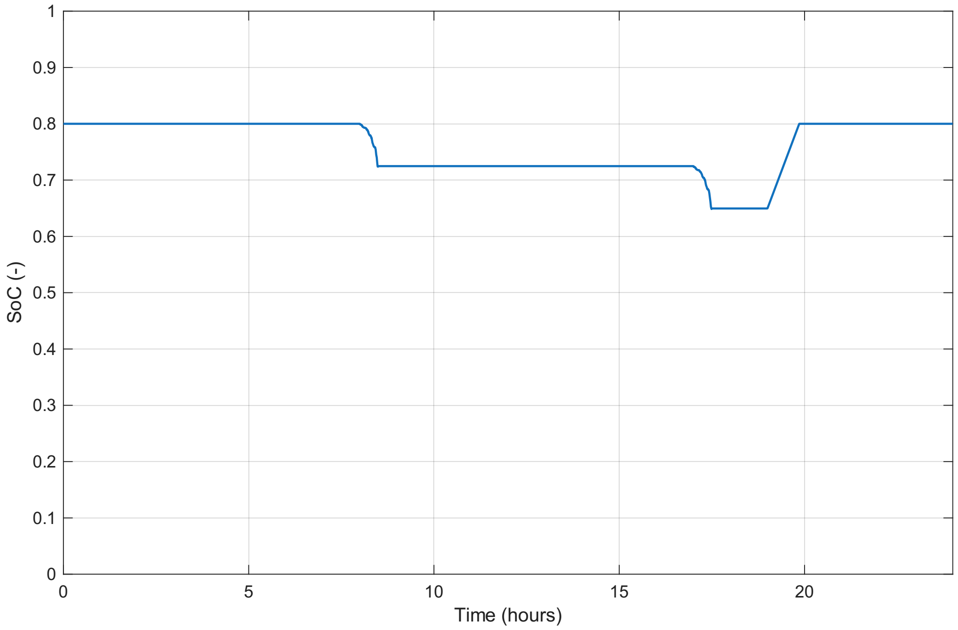

Figure 5.2: SOC profile 1 for a full day

The **2-year profile** was then created by repeating this daily cycle 365*2 times, producing a continuous load pattern suitable for long-term degradation modeling.

5.3.2. Power Profile 2 (Driving, V2G Operation, and Charging)

The daily power profile was developed by combining two WLTP driving cycles, one vehicle-to-grid (V2G) discharge event, and one charging event . This profile represents an extended operating sequence A→B→A→C→A, where the vehicle first returns home, participates in the grid support through V2G operation, and subsequently recharges using a home charger with a rated power of 7.4 kW. Figures 5.3 and 5.4 present the corresponding daily battery power and SOC profiles.

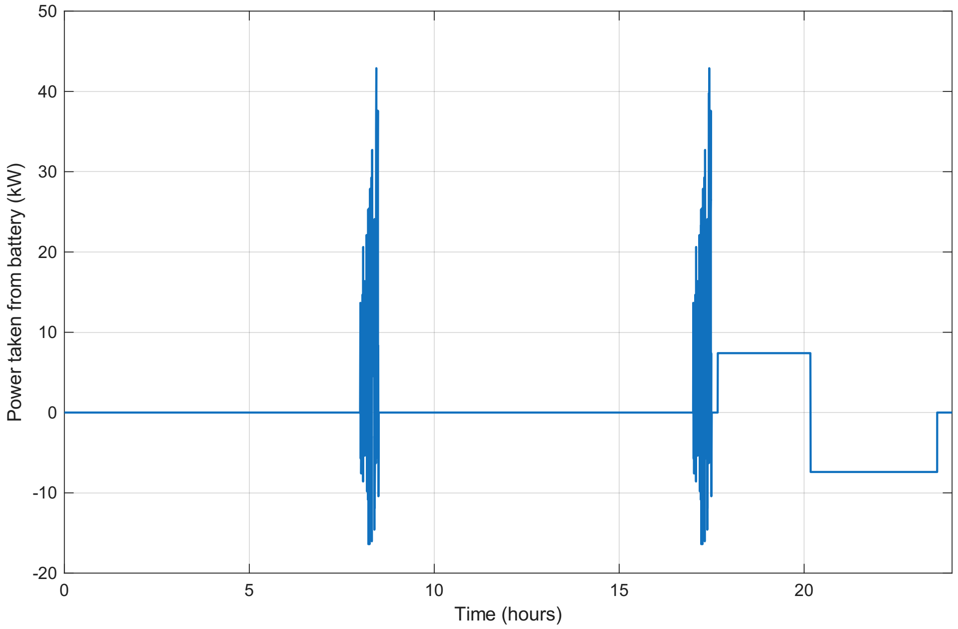

Figure 5.3: Power profile 2 for a full day

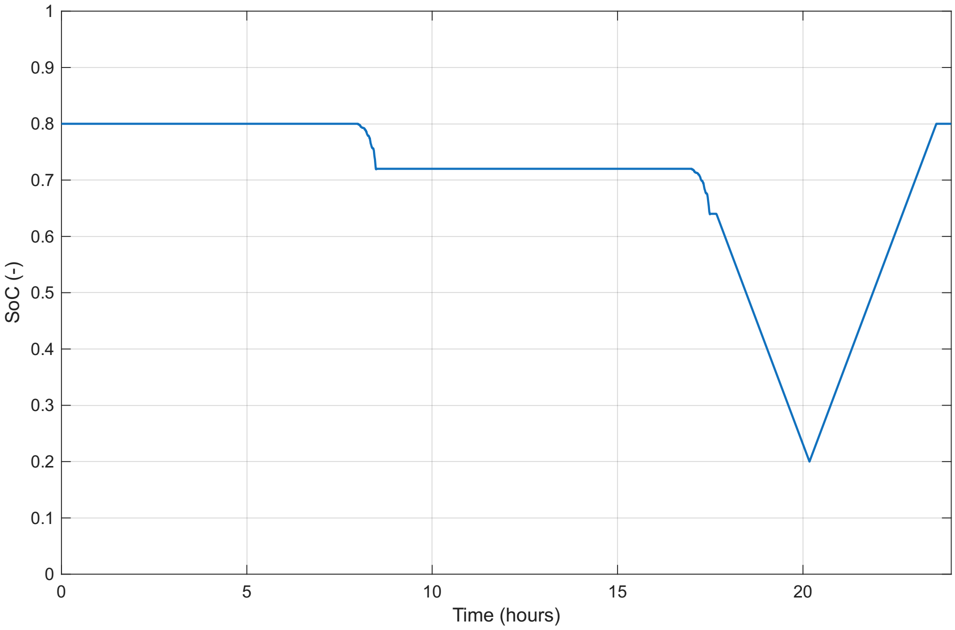

Figure 5.4: SOC profile 2 for a full day

Similarly to the baseline case, this daily profile was repeated 365*2 times to produce a 2-year power profile, allowing consistent and comparable long-term degradation modeling under V2G-enabled operation.

5.3.3. Derived Parameters

From the power profile, several time-dependent parameters were derived, including:

- **Current:** $I = P/V_{\text{batt}}$
- **Distance:** integrated vehicle velocity over time (≈ 23 km per WLTP cycle)
- **Cell throughput:** total energy processed (Ah)
- **C-rate:** $|I|/\text{capacity}$
- **State of Charge (SoC):** obtained by Coulomb counting, with an initial SoC of 50%

5.4. Scenarios

In this study, three operating scenarios are considered. These scenarios are designed to evaluate the degradation behavior of the different battery aging models under varying load conditions.

5.4.1. Scenario 1

In Scenario 1, the cycling degradation of the four battery aging models is evaluated under **the power Profile 1**, which represents the baseline operating condition. The hybrid configuration is described by **Model 4-a**, where the battery pack consists of 90% NMC/Gr cells and 10% NMC/LTO cells.

5.4.2. Scenario 2

In Scenario 2, the same four aging models are simulated using **the Power Profile 2**, which represents a more demanding operating condition compared to Scenario 1. This profile introduces higher stress on the battery system in terms of cycling intensity and load variation. The hybrid battery configuration follows **Model 4-a**, maintaining the same cell proportion as defined in Scenario 1.

5.4.3. Scenario 3

Scenario 3 is also evaluated using **Power Profile 2**. The hybrid system is represented by **Model 4-b**, where the battery pack consists of 85% NMC/Gr cells and 15% NMC/LTO cells. allowing for a comparative assessment of how the proportion of modified LTO cells influences degradation under more demanding operating conditions.

5.5. Simulation Results

The results of the two-year simulation are presented and compared for the three scenarios considered, highlighting the differences in long-term degradation and performance under normal and V2G operating conditions.

5.5.1. Scenario 1

The results of Scenario 1 are presented and analyzed to evaluate the battery degradation and performance under baseline operating conditions, representing normal vehicle operation.

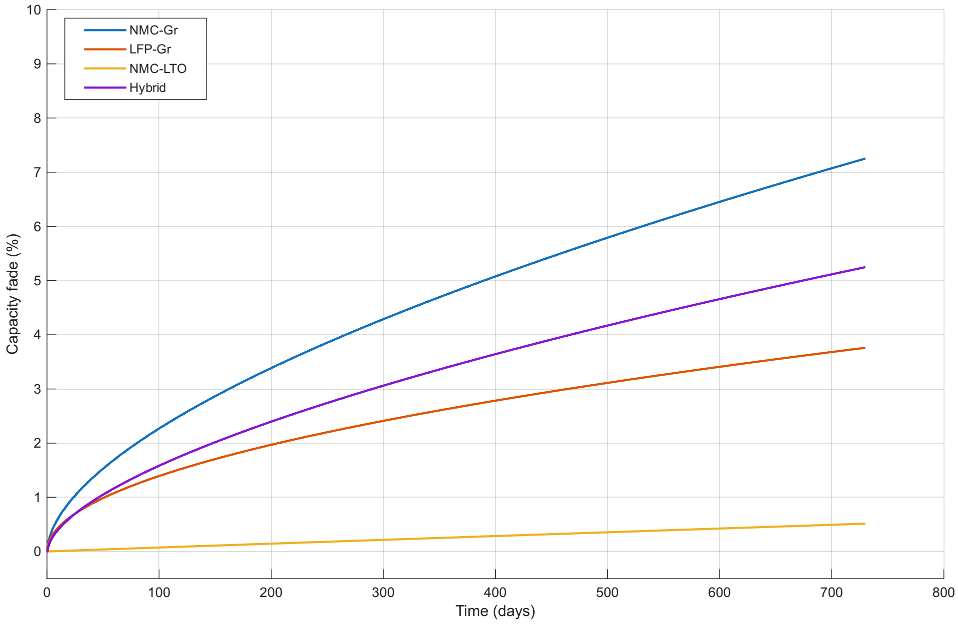

Figure 5.5: Comparative capacity fade of NMC/Gr, LFP/Gr,NMC/LTO, and hybrid battery under Scenario 1 .

Figure 5.5 presents the results of the capacity loss after two years for the battery chemistries investigated under the operating conditions of scenario 1. The Model 1 (NMC/Gr) exhibits the highest capacity loss, reaching 7.525% , indicating a strong sensitivity to cyclic aging. In contrast, Model 2 (LFP/Gr) shows lower degradation with a final capacity fade of 3.76%, while Model 3 (NMC/LTO) demonstrates the best cycling durability, exhibiting the lowest fade of 0.514%. The hybrid configuration (Model 4) results in a moderate capacity loss of 5.248%, corresponding to a reduction of approximately 2.277% compared to pure NMC, due to the buffering effect provided by the 10% % share of (NMC/LTO).

These results clearly highlight the differences in aging behavior among the investigated chemistries under Scenario 1 operating conditions. NMC shows pronounced sensitivity to cycling-related stress, even at a moderate depth of discharge, whereas LFP and LTO maintain substantially better capacity retention due to their enhanced structural stability and lower degradation rates. The hybrid configuration achieves an intermediate aging performance, significantly mitigating the degradation observed in pure NMC.

Overall, LTO provides the best capacity retention, followed closely by LFP, while NMC remains the most degradation-prone chemistry. The hybrid system effectively reduces NMC aging by redistributing part of the cycling stress to the LTO component, thereby improving overall durability compared to standalone NMC operation.

The previous results represent the total degradation accumulated during cycling periods, including both pure cycling aging and calendar aging that occurs simultaneously during cycling. To gain a deeper understanding of the relative influence of these two aging mechanisms in each model, the individual contributions of pure cycling and calendar aging are presented separately and illustrated in the following figures.

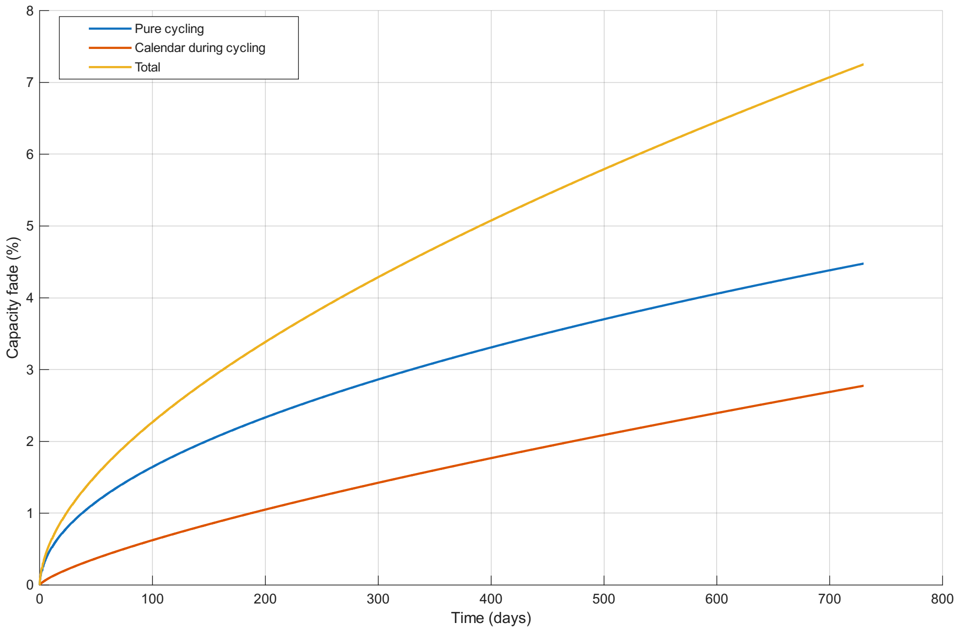

Figure 5.6: Pure cycling aging and calendar aging for NMC/Gr in scenario

Figure 5.6 shows the contribution of pure cycling and calendar aging to the chemistry of NMC/Gr. The pure cycling component reaches 4.476%, while the calendar aging accumulated during cycling periods contributes 2.775% to the total capacity fade. This indicates that although cycling-induced degradation remains the dominant mechanism, calendar aging represents a substantial portion of total fade.

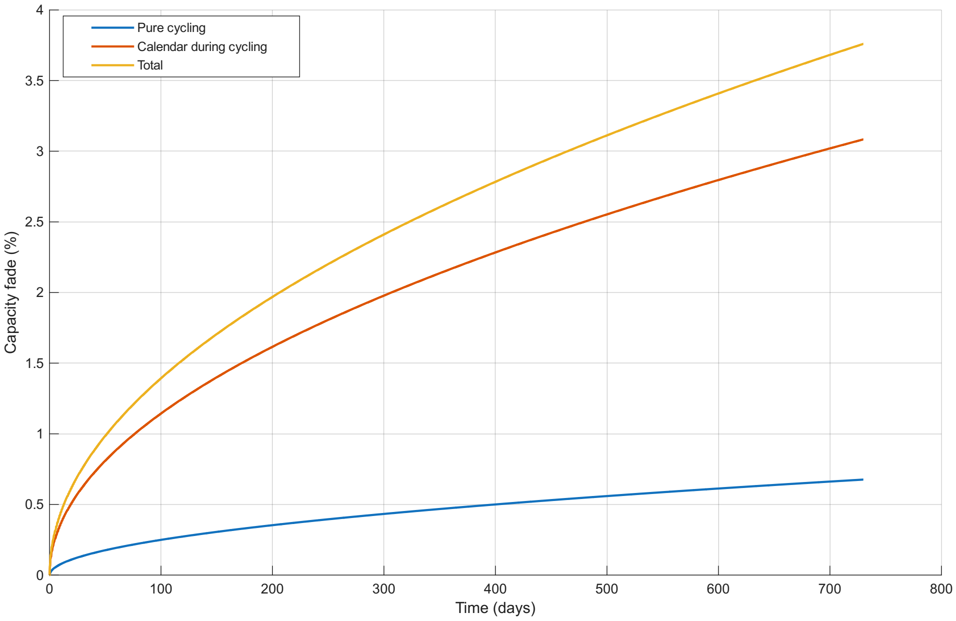

Figure 5.7: Pure cycling aging and calendar aging for LFP/Gr in scenario

Figure 5.7 presents the decomposition of the total capacity loss for the LFP/Gr chemistry. The pure cycling contribution amounts to 0.675%, while calendar aging during cycling periods reaches 3.084%. This clearly indicates that LFP experiences relatively low degradation from cycling itself, but a significantly higher contribution from calendar aging. Unlike NMC/Gr, where cycling degradation dominates. This behavior can be attributed to the higher temperature sensitivity of the LFP calendar aging model. Since calendar degradation during cycling is calculated using the cycling temperature (42.5 °C), the elevated operating temperature significantly accelerates calendar dependent degradation in LFP.

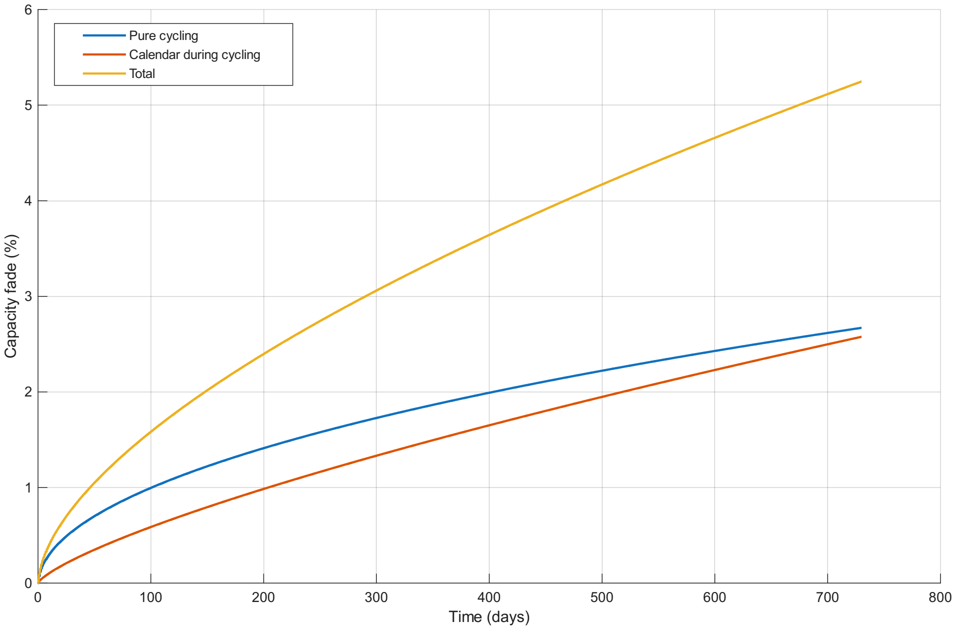

Figure 5.8: Pure cycling aging and calendar aging for Hybrid pack in scenario

Figure 5.8 presents the decomposition of the total capacity loss for the hybrid configuration. The pure cycling contribution reaches 2.67%, while the calendar aging accumulated during cycling amounts to 2.57%. Compared to the pure NMC, the calendar component in the hybrid system remains relatively close to the NMC calendar contribution. In contrast, the pure cycling component is significantly reduced compared to NMC. This reduction is primarily attributed to the presence of LTO within the hybrid architecture, which absorbs part of the cycling stress and exhibits inherently low cycling-induced degradation. As a result, the hybrid system maintains a calendar aging level similar to that of NMC while benefiting from a noticeable decrease in pure cycling degradation due to the buffering effect of the LTO component.

5.5.2. Scenario 2

The results of Scenario 2 are presented and analyzed to assess the impact of vehicle-to-grid (V2G) operation on battery degradation and overall system performance.

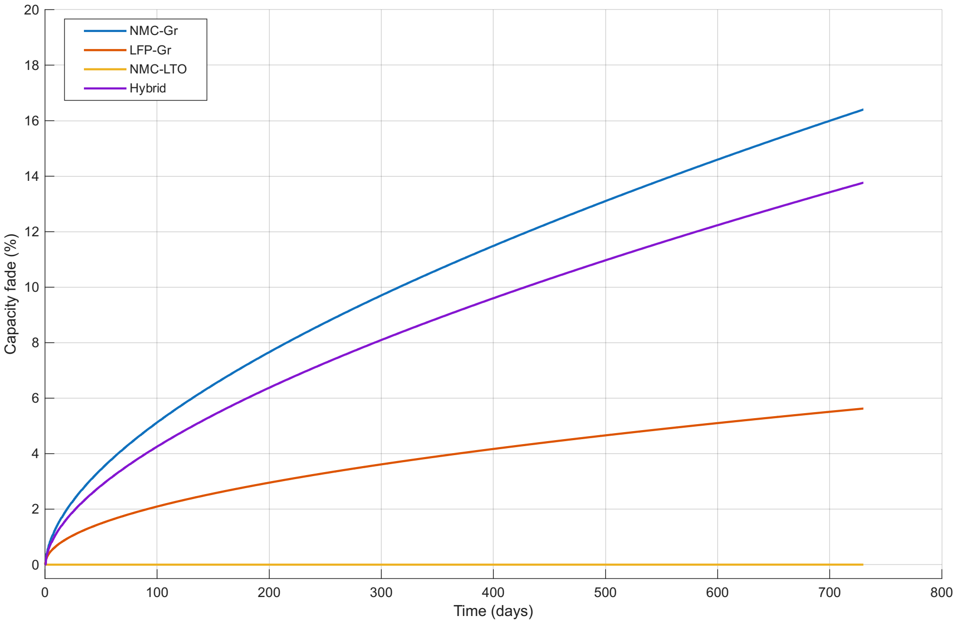

Figure 5.9: Comparative capacity fade of NMC/Gr, LFP/Gr,NMC/LTO, and hybrid battery configurations under Scenario 2

Figure 5.9 shows that Model 1 (NMC/Gr) again exhibits the highest capacity loss, reaching 16.401% , indicating a strong sensitivity to cyclic aging. In contrast, Model 2 (LFP) shows substantially lower degradation with a fading of the final capacity of 5.626%, while Model 3 (NMC/LTO) demonstrates superior cycling durability, showing a negligible fading of approximately 0.002%. The hybrid configuration (Model 4) results in a moderate capacity loss of 13.765%, representing a reduction of approximately 2.656% compared to pure NMC, attributable to the buffering effect of the 10% % LTO share.

These results reflect the impact of the more aggressive operating conditions applied in Scenario 2. The pronounced increase in NMC degradation confirms its high sensitivity to deeper cycling and elevated mechanical and electrochemical stresses under such conditions. Degradation mechanisms such as the loss of lithium inventory (LLI), the loss of active material (LAM), and repeated solid electrolyte interphase (SEI) growth are intensified, leading to accelerated capacity fading. LFP also exhibits increased degradation compared to Scenario 1; however, absolute capacity loss remains acceptable, highlighting its structural stability and intrinsic robustness under demanding cycling conditions. In contrast,

LTO shows a fundamentally different aging response. The almost negligible capacity fade observed demonstrates its strong resistance to lithium plating, limited SEI formation, and structural degradation, even under aggressive operation.
In general, Scenario 2 clearly differentiates the aging behavior of the investigated chemistries: LTO provides the best durability, LFP maintains stable and moderate degradation, and NMC experiences the most severe capacity loss. The hybrid system partially mitigates NMC degradation, confirming the beneficial buffering contribution of the LTO component under harsh operating conditions.

Similarly to Scenario 1, the individual contributions of pure cycling and calendar aging are separately analyzed and presented in the following figures.

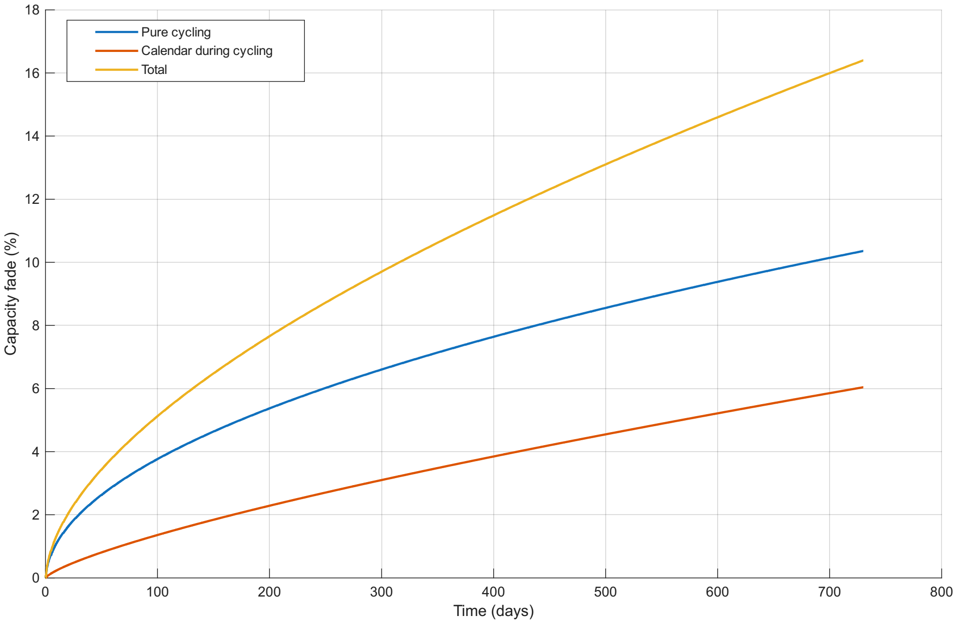

Figure 5.10: Pure cycling aging and calendar aging for NMC/Gr in scenario 2

Figure 5.10 shows the decomposition of the total capacity loss for the chemistry of NMC/Gr under scenario 2. The contribution of pure cycling increases significantly to 10.358%, while calendar aging during cycling reaches 6.043%. Cycling-induced degradation remains the dominant mechanism; however, the calendar component also becomes substantial under more aggressive operating conditions.

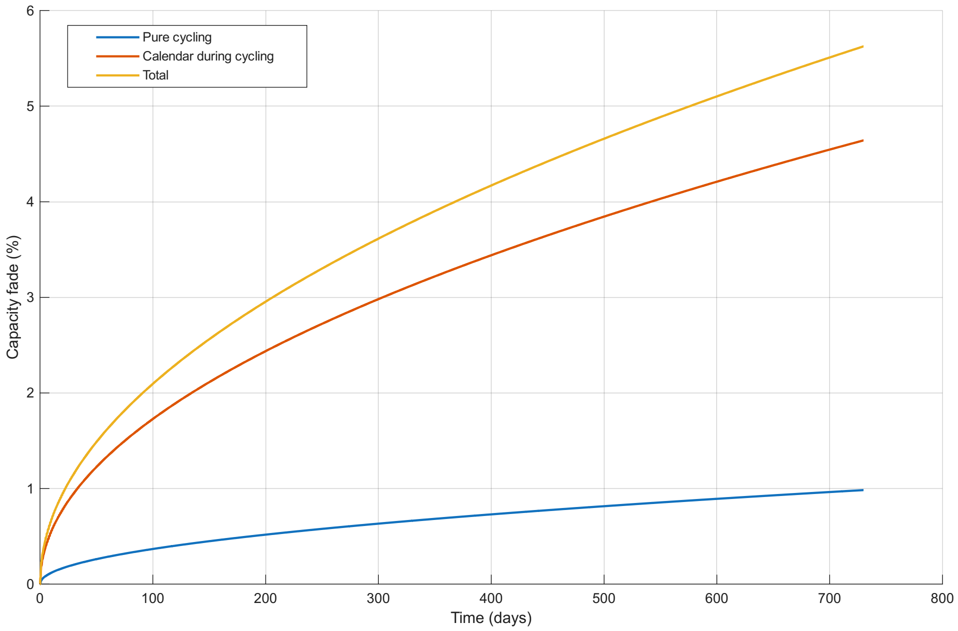

Figure 5.11: Pure cycling aging and calendar aging for LFP/Gr in scenario 2

Figure 5.11 presents the decomposition of LFP/Gr under Scenario 2. The pure cycling contribution remains very low at 0.983%, while calendar aging reaches 4.642%. Similarly to Scenario 1, LFP degradation is clearly governed by calendar aging rather than cycling-induced mechanisms. The very low pure cycling fade confirms the structural robustness of LFP, while the relatively high calendar contribution highlights the strong temperature dependence of the LFP calendar aging model.

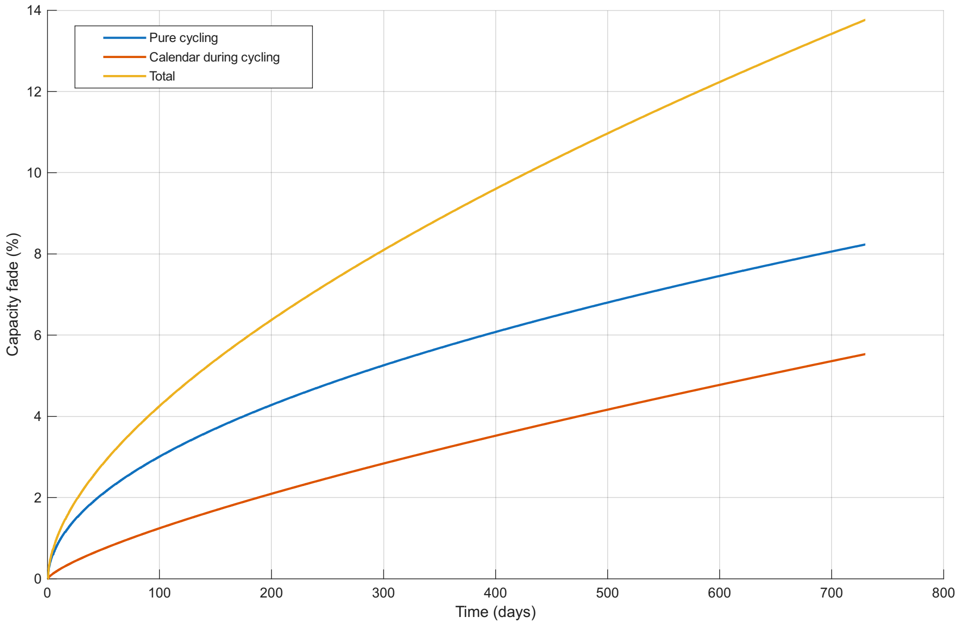

Figure 5.12: Pure cycling aging and calendar aging for Hybrid pack in scenario 2

Figure 5.12 illustrates the degradation decomposition for the hybrid configuration in scenario 2. Pure cycling contributes 8.231%, while calendar aging accounts for 5.533%. However, the calendar component remains close to that of the NMC. However,the contribution of pure cycling is noticeably reduced compared to the pure NMC (10.358%), demonstrating the mitigating effect of the LTO component. By absorbing part of the cycling stress, LTO reduces the intensity of cycle-induced degradation.

5.5.3. Scenario 3

The results of Scenario 3 are presented and analyzed to examine the effect of V2G operation while also investigating the sensitivity to increasing the share of the NMC/LTO battery within the hybrid configuration.

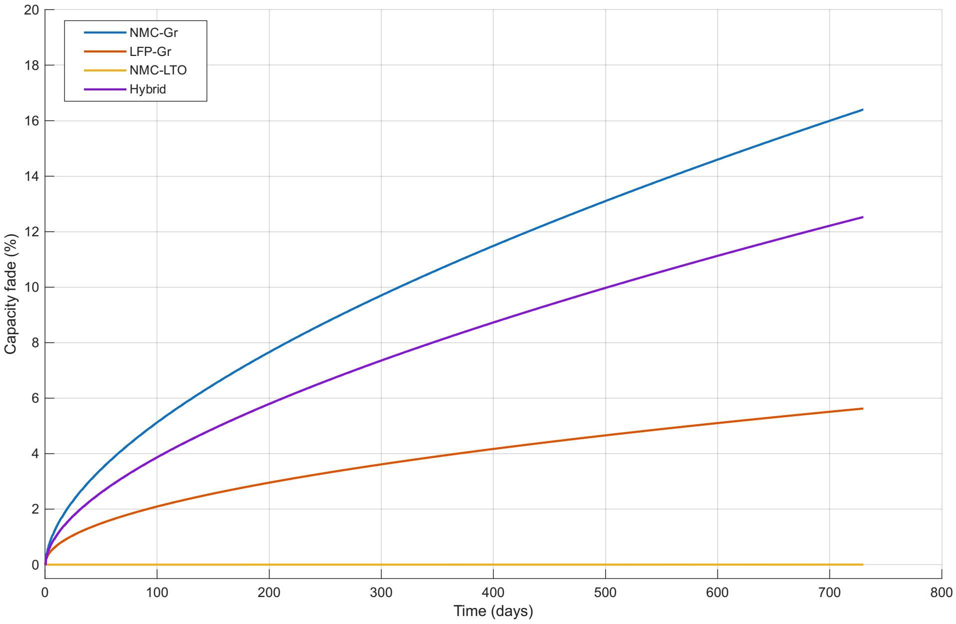

Figure 5.13: Comparative capacity fade of NMC/Gr, LFP/Gr,NMC/LTO, and hybrid battery configurations under Scenario 3

Figure 5.13 shows that the degradation results of Model 1 (NMC/Gr), Model 2 (LFP/Gr), and Model 3 (NMC/LTO) in Scenario 3 are identical to those observed in Scenario 2. In contrast, the fade of the hybrid configuration (Model 4-b) is 12.53 and exhibits a reduced capacity fade of 1.235% compared to the hybrid result in Scenario 2 , which corresponds to a reduction attributable to the increase in the share of LTO. highlighting the enhanced buffering effect provided by the higher fraction of LTO.

Overall, in Scenario 3, LTO again achieves the best capacity retention, followed by LFP, while NMC remains the chemistry most susceptible to degradation.The results demonstrate that, while operational strategies may not significantly alter intrinsic chemistry aging, they play a critical role in enhancing durability at the system level, particularly in hybrid configurations.

Since the operating conditions for NMC/Gr and LFP/Gr in Scenario 3 are identical to those in Scenario 2,only the contributions of pure cycling and calendar aging in the hybrid configuration are separately analyzed and presented in the following figure.

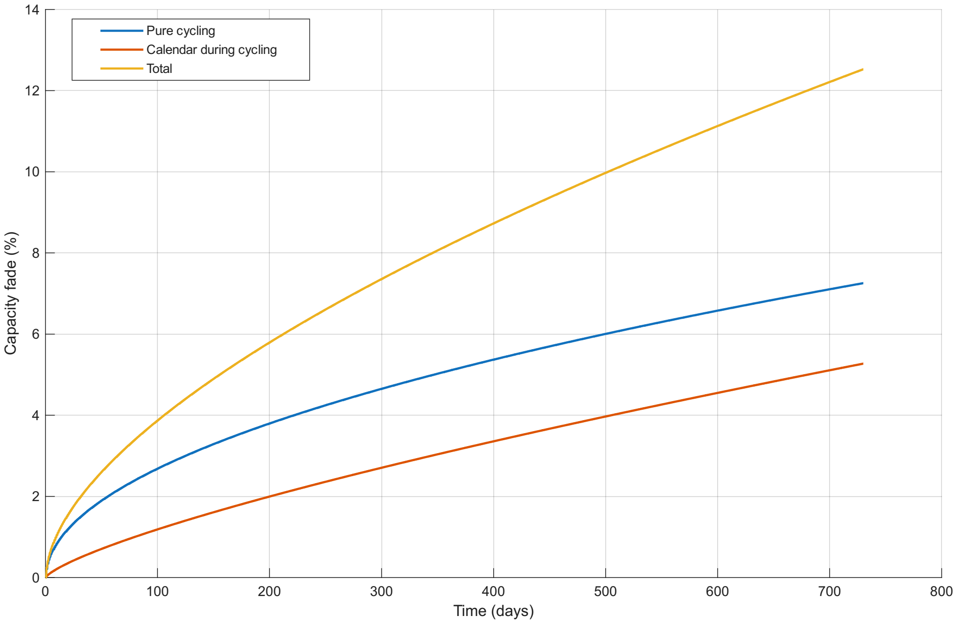

Figure 5.14: Pure cycling aging and calendar aging for Hybrid pack in scenario 3

Figure 5.14 presents the decomposition of the total capacity loss for the hybrid configuration in scenario 3. The pure cycling contribution amounts to 7.255%, while calendar aging during cycling reaches 5.272%. Compared to Scenario 2 (8.231% cycling and 5.533% calendar), both degradation components are slightly reduced in Scenario 3. The decrease in pure cycling degradation is more pronounced, indicating that the modified utilization strategy and the increase in LTO share effectively mitigate cycle-induced stress on the NMC component. Although the calendar contribution remains close to that observed in Scenario 2, it is still primarily governed by the NMC fraction operating at elevated temperature.
The reduction in cycling-induced degradation, combined with a moderate decrease in calendar aging, demonstrates that improved sharing within the hybrid architecture can enhance overall durability.

5.6. Cross scenarios comparison

A cross-scenarios comparison of the simulation results is performed to evaluate the differences in battery degradation and performance under the considered operating conditions. The comparison highlights the influence of the different battery configurations and operating strategies.

Table 5.3: Capacity fade after two years

Scenario	NMC (%)	LFP (%)	LTO (%)	Hybrid (%)
Scenario 1	7.252	3.76	0.514	5.248
Scenario 2	16.401	5.626	0.002	13.765
Scenario 3	16.401	5.626	0.002	12.530

Table 5.3 summarizes the simulated loss of capacity of each battery chemistry after two years of operation in the three investigated scenarios. A comparison between Scenario 1 and the more aggressive Scenarios 2 and 3 reveals a pronounced increase in the severity of degradation, particularly for NMC. Its fading capacity increases from 7.252% in Scenario 1

to 16.401% in Scenarios 2 and 3, corresponding to an increase of approximately 126%.This substantial increase highlights the strong sensitivity of the NMC chemistry to intensified operating conditions. Accelerated degradation is associated with the amplification of key aging mechanisms such as loss of lithium inventory (LLI), loss of active material (LAM), and repeated growth of the solid electrolyte interphase (SEI) under elevated electrochemical stress.

LFP follows a similar trend, but with considerably lower severity. Its fade capacity increases from 3.76% in Scenario 1 to 5.626% in Scenarios 2 and 3, representing an increase of approximately 49.6%. Although degradation intensifies under more demanding conditions, the absolute fade remains significantly lower than that of NMC, reflecting the structural robustness and electrochemical stability of the LFP cathode materials.

In contrast, LTO exhibits distinct aging behavior.When moving from Scenario 1 to the more severe Scenarios 2 and 3, its capacity to fade decreases from 0.514% to approximately 0.002%, which is practically negligible.

This behavior can be attributed to several factors. First, increasing the active surface area of the active electrode during the early stages of cycling, as discussed in 4.3, may contribute to the observed degradation pattern. This effect becomes more pronounced when the cycling depth is greater, as in Scenarios 2 and 3, where more intensive battery usage enhances electrochemical activation processes. Second, although the individual contributions of pure cycling and calendar aging were not analyzed separately for the NMC/LTO system due to the lack of available calendar aging data, certain observations can still be made. In Scenario 1, where the state of charge (SoC) remains relatively high during cycling, the overall degradation is greater compared to scenario 2 and 3, where the SoC operates at lower levels due to more aggressive battery usage. This suggests that higher average SoC conditions may intensify calendar-related degradation mechanisms and contribute more significantly to total capacity fade.

The hybrid configuration shows a strong dependence on both the operating severity and the system-level utilization strategy. Moving from Scenario 1 to Scenario 2, the hybrid capacity fade increases from 5.248% to 13.765%, largely driven by the dominant contribution of the NMC component. However, in Scenario 3, where the LTO share is increased, hybrid degradation is reduced to 12.53%, indicating a partial mitigation of aging through improved power sharing. Although the reduction is moderate, it demonstrates the beneficial effect of incorporating a more durable chemistry within the hybrid architecture.

Overall, the results reveal a clear hierarchy of aging performance. NMC remains the most sensitive chemistry under aggressive cycling conditions, LFP maintains moderate and comparatively stable degradation, and LTO demonstrates exceptional stability with almost negligible fade under intensive scenarios. The hybrid system leverages the complementary characteristics of NMC and LTO: while NMC provides high energy density, LTO acts as a stabilizing component that redistributes electrochemical stress and enhances overall durability. These findings underscore the importance of both the selection of chemicals and the operational strategy in battery system design, particularly for applications that involve frequent and demanding cycling such as V2G operation.

5.7. Economic perspective

In addition to technical performance, the economic implications of battery degradation are critical to evaluating the feasibility of V2G participation. Therefore, an economic assessment is performed to estimate the degradation-related cost associated with each battery configuration.

The economic impact of battery aging is evaluated using a degradation cost model that directly relates capacity fading to the initial cost of the battery system. The degradation cost is expressed as:

$$C_{\text{deg}} = E_{\text{pack}} \, C_{\text{s/kWh}} \, f \tag{5.13}$$

where:

- C_{deg} the total degradation cost (USD).
- E_{pack} the installed battery energy capacity (kWh).
- $C_{\text{s/kWh}}$ the cost of the battery pack per unit of energy capacity (USD/kWh).
- f the capacity fade.

For the hybrid battery system, the degradation cost is computed using a capacity-weighted formulation:

$$C_{\text{deg,hyb}} = E_{\text{pack}} \sum_{i} \alpha_i \, C_{\text{s/kWh},i} \, f_{\text{hyb}} \tag{5.14}$$

where:

- α_i the installed capacity fraction of chemistry i, with $\sum \alpha_i = 1$.
- f_{hyb} the total hybrid system capacity fade.

In this study, the battery capacity is fixed at $E_{\text{pack}} = 42.2$ kWh. Battery cost values $C_{\text{s/kWh}}$ are taken from Table 3.5. In particular, the costs of the NMC and LFP pack are 65 and 50 USD / kWh, respectively, while the cost of the LTO-based pack is reported as 200 USD / kWh. f and f_{hyb} taken from Table 5.3.

The total degradation cost of individual and hybrid battery systems in the three operating scenarios is summarized in Table 5.4.

Table 5.4: Total degradation cost for individual and hybrid battery systems after 2 years of operation

System	**Scenario 1 (USD)**	**Scenario 2 (USD)**	**Scenario 3 (USD)**
NMC	200	500	500
LFP	80	120	120
LTO	45	0.2	0.2
Hybrid	175	456	450

From a cost perspective, noticeable differences are observed among the considered chemistries due to variations in both the degradation rate and the cost per kWh. In Scenario 1, NMC results in a degradation cost of 200 USD, while LFP shows a significantly lower cost of 80 USD, which represents approximately 60% lower degradation cost compared to NMC. LTO, despite its high cost per kWh, yields a degradation cost of 45 USD in Scenario 1, primarily due to its very low capacity decline.

Under the more demanding operating conditions of Scenario 2, the degradation cost of

NMC increases substantially to 500 USD, reflecting its higher sensitivity to intensive cycling. In comparison, LFP reaches 120 USD, which is nearly 74% lower than NMC under the same conditions. LTO shows a negligible degradation cost of approximately 0.17 USD due to its minimal capacity fade in this scenario.

Similar trends are observed in Scenario 3, where NMC maintains a high degradation cost of 500 USD, LFP remains at 120 USD, and LTO stays close to zero.

The economic assessment highlights that the degradation cost is determined by the combined effects of capacity fade and chemistry-specific investment costs. While LTO demonstrates superior cycling stability with minimal capacity degradation, its high cost per kWh limits the economic advantage gained from its low aging rate. In contrast, NMC systems incur the highest degradation cost in all scenarios, primarily due to greater capacity loss under demanding operating conditions. LFP shows the most economically favorable behavior among the chemistries, as its moderate degradation, combined with a lower cost per unit energy, results in comparatively low overall degradation costs.

The hybrid configuration in Scenarios 1 and 2, where the battery pack consists of 90% NMC. the degradation cost closely follows the trend of NMC. This indicates that the economic benefit of hybridization remains limited when the more degradation-prone chemistry dominates the pack composition. In Scenario 3, increasing the LTO share to 15% reduces the fading of overall capacity and leads to a modest improvement in economic performance compared to the other hybrid cases. However, compared to LFP, the hybrid system still exhibits higher degradation costs.

Overall, from a strictly degradation-cost perspective, LFP remains the most cost-effective solution under the operating conditions studied.The hybrid approach may become attractive when high power capability or enhanced operational robustness is required.

Battery chemistry also affects vehicle performance through differences in gravimetric energy density, which lead to variations in battery pack mass. This difference in mass represents an additional factor that can influence overall system performance and vehicle efficiency.

The battery pack mass is approximated as

$$m \approx \frac{E_{\text{pack}}}{e_g} \tag{5.15}$$

where

- e_g is the gravimetric energy density (Wh/kg).

For hybrid configurations, the total pack mass is estimated as:

$$m_{\text{hyb}} \approx \frac{\alpha_{\text{NMC}} E_{\text{pack}}}{e_{g,\text{NMC}}} + \frac{\alpha_{\text{LTO}} E_{\text{pack}}}{e_{g,\text{LTO}}}. \tag{5.16}$$

The estimated mass of the pack is reported in Table 5.5.

Table 5.5: Estimated battery pack mass and energy density

Chemistry / configuration	**Energy density (Wh/kg)**	**Estimated mass (kg)**
NMC	165	255
LFP	120	352
LTO	74	570
Hybrid (10% LTO / 90% NMC)	(NMC, LTO)	287
Hybrid (15% LTO / 85% NMC)	(NMC, LTO)	303

From a mass perspective, significant differences appear between the considered chemistries as a result of their varying energy densities. NMC exhibits the lowest pack mass (255 kg), reflecting its high gravimetric energy density. LFP results in a substantially higher pack mass (352 kg), approximately 38% heavier than NMC for the same installed energy capacity. LTO shows the largest mass (570 kg), more than double that of NMC, which directly reflects its low energy density.
Hybrid configurations provide an intermediate solution. The 10% LTO / 90% NMC hybrid increases the pack mass to 287 kg, representing a 12.5% increase compared to pure NMC, but is still significantly lighter than LFP. Increasing the LTO fraction to 15% raises the mass further to 303 kg, corresponding to a 19% increase relative to NMC. Although hybrid systems improve durability compared to pure NMC, this benefit comes at the expense of additional mass, which can negatively affect vehicle efficiency and driving range.

When weight is considered alongside degradation cost, an important trade-off becomes evident. While LFP offers a lower degradation cost, it imposes a considerable weight penalty compared to NMC and hybrid configurations. In contrast, LTO-based systems, despite their excellent durability, introduce substantial mass increases that may not be practical for vehicle applications. Therefore, the optimal configuration depends on the specific design priority: energy efficiency and driving range favor NMC, economic degradation resilience favors LFP, and operational robustness with moderate mass penalty may justify a hybrid approach.

6

Conclusions

6.1. (NMC/LTO) Degradation Model

Based on the successive refinement steps presented in **??**, the final empirical degradation model for lithium titanate oxide (LTO) batteries, incorporating both cycle depth and current rate effects, is expressed as follows.

$$\boxed{C_{\textbf{fade}} = 0.999 \cdot e^{-(0.648\,cd+0.918\,c_r)} \cdot FEC^{(0.044\,cd^{1.120}\cdot 1.049\,c_r^{-0.007})}}$$

This model describes capacity fade as a function of full equivalent cycles (FEC), cycle depth (cd), and current rate (c_r), using a power-law formulation with physically interpretable parameters.

The results demonstrate that the proposed model successfully captures the dominant degradation trends of lithium titanate oxide (LTO) batteries at different aging stages. By incorporating two key stress factors—cycle depth and current rate—the model is capable of providing degradation predictions under a wide range of operating conditions. The model accurately represents capacity decline during the early and mid-life regions and offers reasonable predictions of end-of-life behavior. Although reduced accuracy is observed for certain combinations of cycle depth and current rate, these deviations are mainly attributed to limitations in the available experimental data and to interaction effects between stress factors. Nevertheless, the overall predictive accuracy remains acceptable and provides meaningful insights into the degradation behavior of (NMC/LTO).

In general, the developed model provides a computationally efficient and physically meaningful framework to predict capacity loss in LTO-based batteries under varying operating conditions. This makes it well suited for long-term simulations and for evaluating battery degradation under both conventional driving and Vehicle-to-Grid (V2G) operation.

6.2. Comparative Analysis

The comparative analysis conducted in this study demonstrates clear and consistent differences in degradation behavior between the lithium-ion battery chemistries investigated under both conventional driving and V2G operation. In all scenarios, NMC/Gr exhibited the highest sensitivity to increased cycling demand and deeper discharge depth, confirming its vulnerability to aggressive operating conditions. Although it offers a high energy density and relatively low upfront cost, its degradation accelerates significantly with increasing usage, leading to substantial long-term capacity loss.

LFP/Gr showed a considerably more stable aging response. Although degradation increased

under more demanding scenarios, the overall capacity fade remained moderate, highlighting the structural and electrochemical robustness of LFP cathode materials. This confirms LFP as a balanced alternative for applications requiring improved durability without a significant cost or mass penalty.
NMC/LTO demonstrated fundamentally different aging characteristics. Under all operating conditions, including aggressive cycling and participation in V2G, exhibited negligible capacity degradation. This superior cycling stability is attributed to its zero-strain anode structure, suppression of lithium plating, and minimal solid electrolyte interphase formation. These characteristics make LTO particularly suitable for high-power and bidirectional grid applications. However, its relatively low energy density, higher cost, and increased pack mass limit its feasibility as a standalone battery chemistry for mainstream electric vehicle applications.
The hybrid configurations (NMC/LTO , NMC/Graphite) effectively combine the advantages of the respective chemistries. By integrating a modest fraction of NMC/LTO, the hybrid system reduces overall degradation compared to NMC/Graphite. The sensitivity analysis between 10% and 15% LTO share demonstrated that even a small increase in the LTO fraction can substantially enhance long-term durability while maintaining acceptable system-level cost and mass.

Overall, the results confirm that the selection of battery chemistry for electric vehicle and V2G applications requires a comprehensive trade-off between degradation behavior, economic cost, and energy density. While NMC/Gr offers high energy density and a competitive upfront cost, it is prone to pronounced degradation. LFP/Gr provides a more economically resilient and degradation-stable alternative, particularly under frequent participation in V2G, although at the expense of increased pack mass. NMC/LTO exhibits exceptional durability and operational robustness, but its higher cost and significantly lower gravimetric energy density restrict its viability as a standalone solution. Hybrid configurations present a practical compromise, showing that even modest LTO integration can noticeably reduce cycling-induced degradation while maintaining acceptable system-level cost and mass.

7

Limitations and Recommendations

7.1. (NMC/LTO) Model

7.1.1. Limitations

Despite the strengths of the proposed degradation model, several limitations should be acknowledged.

1. **Limited data availability and reliance on digitized datasets**
   The availability of experimental data was limited and the datasets used for model development were obtained by digitizing published figures rather than by direct access to raw measurements. These factors constrained parameter identification and introduced additional uncertainty due to resolution limits and potential digitization errors, resulting in an overall predictive accuracy of approximately 70%.

2. **Restricted validity across operating conditions**
   The model performs best within the operating conditions most strongly represented in the data set, particularly at a cycle depth of $cd = 50\%$ and a current rate of $C_r = 2$. Although acceptable performance is observed across different cycle depths, this is not the case for variations in current rate. In particular, at high numbers of full equivalent cycles, model predictions deviate noticeably from experimental behavior, leading to insufficient accuracy.

3. **Limited operating temperature range**
   The model was developed using experimental data obtained at a single operating temperature of 42.5 °C. Consequently, the influence of temperature on degradation behavior is not captured, limiting the applicability of the model across a wider temperature range.

4. **Exclusion of calendar aging effects**
   The proposed model exclusively addresses degradation occurring during active cycling and does not incorporate capacity fade associated with non-operational periods (calendar aging). In real-world applications, especially under Vehicle-to-Grid (V2G) operation , calendar aging may contribute significantly to overall degradation.

7.1.2. Recommendations

Based on the identified limitations, several recommendations are proposed to improve the accuracy, robustness, and applicability of the degradation model in future work.

First, Future studies should incorporate a broader and more comprehensive experimental dataset, ideally with direct access to raw measurement data. In addition, the model development should rely on experimental data covering a wider range of operating conditions, including multiple depths of discharge and current rates. Expanding the data set in this manner would reduce uncertainty in parameter estimation and enhance the predictive accuracy of the model.

Second, temperature-dependent degradation data should be included to explicitly capture the influence of thermal conditions on capacity fade. Incorporating temperature as an additional stress factor would extend the validity of the model across a wider range of operating environments relevant to electric vehicles and grid-interactive applications.

Third future model developments should integrate calendar aging effects alongside cycle-induced degradation. Including time-dependent aging would enable more realistic lifetime prediction under operating profiles that involve significant idle periods, such as Vehicle-to-Grid (V2G) operation.

Overall, implementing these recommendations would lead to a more comprehensive and transferable degradation modeling framework, improving its suitability for long-term battery lifetime assessment and system-level optimization studies.

7.2. Comparative Analysis

7.2.1. Limitations

The present study is subject to several limitations.

1. **Simplified power profiles**
   The applied power profiles are based on repeated WLTP driving cycles and predefined V2G operation. Although suitable for controlled comparison, more realistic usage patterns, including varying driving habits, weekend behavior, irregular travel distances, and seasonal variation, could provide a more representative long-term degradation assessment.

2. **Constant temperature assumption**
   The simulations were conducted using a fixed operating temperature, which does not reflect realistic thermal fluctuations during driving, charging, and V2G operation. In real applications, the temperature varies spatially within the pack and temporally with operating conditions, influencing both the cycle and the calendar aging rates. Defining thermal gradients and dynamic heat generation may therefore limit the accuracy of long-term degradation estimation.

3. **Battery pack mass effects**
   The influence of battery pack mass on vehicle performance was not dynamically incorporated into the simulation. Although gravimetric energy density was used to estimate the mass of the pack, its impact on energy consumption, driving range, and overall system efficiency was not explicitly modeled.

7.2.2. Recommendations

Future studies should address several important aspects to further enhance the scope and accuracy of this work.

First, calendar aging effects should be included in addition to cyclic aging. Since calendar aging represents a significant contributor to overall battery degradation, particularly during long storage periods, incorporating it would enable more accurate long-term lifetime prediction and end-of-life estimation.

Second, hybrid power-sharing strategies should be optimized using control-oriented algorithms. In particular, primarily assigning high-power demand to the NMC/LTO, while reserving the NMC/Gr component for energy-dominant operation, could further enhance the durability and performance of the system. This approach is especially relevant under V2G operation, where power fluctuations are frequent and demanding.

Third, Future work could extend the analysis by investigating alternative hybrid battery configurations, such as LTO–LFP systems, which may strengthen the comparative evaluation of hybrid battery architectures and their degradation behavior.

Fourth, a potential extension of this work is the integration of thermal effects into the simulation framework to analyze temperature distribution and its influence on battery degradation.

Bibliography

[1] W. Kempton and J. Tomic, “Vehicle-to-grid power fundamentals: Calculating capacity and net revenue,” *Journal of Power Sources*, vol. 144, no. 1, pp. 268–279, 2005. [Online]. Available: https://www-sciencedirect-com.tudelft.idm.oclc.org/science/article/pii/S0378775305000352?casa_token=h4s0sNwoSbMAAAAA:DKaJgxPFZEbS4KjiYHRNr8ZY9HtUzTHLooB6O2n0vaml3XC_2zYQJBR9jr1kEfV0iEPSyvFkYek

[2] K. Uddin *et al.*, “The viability of vehicle-to-grid operations from a battery technology and policy perspective,” *Energy*, vol. 145, pp. 1–12, 2018. [Online]. Available: https://www-sciencedirect-com.tudelft.idm.oclc.org/science/article/pii/S0301421517307619#s0090

[3] J. Wang, J. Purewal, P. Liu, J. Hicks-Garner, S. Soukazian, E. Sherman, A. Sorenson, L. Vu, H. Tataria, and M. W. Verbrugge, “Degradation of lithium ion batteries employing graphite negatives and nickel–cobalt–manganese oxide+ spinel manganese oxide positives: Part 1, aging mechanisms and life estimation,” *Journal of Power Sources*, vol. 269, pp. 937–948, 2014. [Online]. Available: https://www-sciencedirect-com.tudelft.idm.oclc.org/science/article/pii/S037877531401074X?via%3Dihub

[4] J. Nájera, J. Arribas, R. De Castro, and C. Núñez, “Semi-empirical ageing model for lfp and nmc li-ion battery chemistries,” *Journal of Energy Storage*, vol. 72, p. 108016, 2023.

[5] Y.-J. Lee, H.-Y. Choi, C.-W. Ha, J.-H. Yu, M.-J. Hwang, C.-H. Doh, and J.-H. Choi, “Cycle life modeling and the capacity fading mechanisms in a graphite/lini0. 6co0. 2mn0. 2o2 cell,” *Journal of Applied Electrochemistry*, vol. 45, no. 5, pp. 419–426, 2015. [Online]. Available: https://link-springer-com.tudelft.idm.oclc.org/article/10.1007/s10800-015-0811-6

[6] A.-I. Stroe, D.-L. Stroe, V. Knap, M. Swierczynski, and R. Teodorescu, “Accelerated lifetime testing of high power lithium titanate oxide batteries,” in *2018 IEEE Energy Conversion Congress and Exposition (ECCE)*. IEEE, 2018, pp. 3857–3863. [Online]. Available: https://ieeexplore-ieee-org.tudelft.idm.oclc.org/abstract/document/8557416/?casa_token=vVraYpzQVCMAAAAA:IDX6fqOy83pAFMPtKqyp_ZF-vZVt_tU2O5G5wMDEuVmh8rJtgH3YU0cm4Z82lBowMjfnTY-yIIQ

[7] M. Soltani, S. B. Vilsen, A.-I. Stroe, V. Knap, and D.-I. Stroe, “Degradation behaviour analysis and end-of-life prediction of lithium titanate oxide batteries,” *Journal of Energy Storage*, vol. 68, p. 107745, 2023. [Online]. Available: https://www-sciencedirect-com.tudelft.idm.oclc.org/science/article/pii/S2352152X23011428?casa_token=gAMC-wkfWswAAAAA:2M-urQJKU3wqePGFkkdr3WKZ4C0xZPZEvCjwksxlJfezBoxtl16b8wfPRoDQnn3UGupMjM_AXY0

[8] D. Wang, J. Coignard, T. Zeng, C. Zhang, and S. Saxena, “Quantifying electric vehicle battery degradation from driving vs. vehicle-to-grid services,” *Journal of Power Sources*, vol. 332, pp. 193–203,

2016. [Online]. Available: https://www-sciencedirect-com.tudelft.idm.oclc.org/science/article/pii/S0378775316313052?casa_token=53OUXraaLksAAAAA:0129Zqxqm1LSzvXlVs6ZKuZm0JDk1cz45IJsMaKQmHUjccf3kG6q4M7YbfyrU6sZWJ_ibiajmw4

[9] T. Lehtola, “Vehicle-to-grid applications and battery cycle aging: A review,” *Renewable and Sustainable Energy Reviews*, vol. 208, p. 115013, 2025. [Online]. Available: https://www-sciencedirect-com.tudelft.idm.oclc.org/science/article/pii/S1364032124007391?casa_token=KGccqmuYC_gAAAAA:KkRqbyLQAVZIDKRbp926wRoEmtHr_btCQZwgDhur6umSeXtICf91wKA5qVi4czMA9Qmep7QAt1w

[10] W. Zhuang, J. Ye, Z. Song, G. Yin, and G. Li, “Comparison of semi-active hybrid battery system configurations for electric taxis application,” *Applied Energy*, vol. 259, p. 114171, 2020. [Online]. Available: https://www-sciencedirect-com.tudelft.idm.oclc.org/science/article/pii/S0306261919318586?casa_token=hj_DZreHPloAAAAA:fNIxhFCjyzy23no-qZutmAL_gTxe10HRZAmJ3VakxGCQnZ7rggAu1KTG4uPlsITsW-NgHA-pW6U

[11] R. Wegmann, V. Döge, and D. U. Sauer, “Assessing the potential of a hybrid battery system to reduce battery aging in an electric vehicle by studying the cycle life of a graphite nca high energy and a lto metal oxide high power battery cell considering realistic test profiles,” *Applied Energy*, vol. 226, pp. 197–212, 2018. [Online]. Available: https://www-sciencedirect-com.tudelft.idm.oclc.org/science/article/pii/S0306261918308225?casa_token=FAhPkOnysgAAAAAA:GV64PU-yMBhOuwTHLovgsJo_EYFHpudU8Mkq6gQLFdsd0SuL7T42r31uAmVk1URcyTPg-iGjhKo

[12] M. Akbarzadeh, J. De Smet, and J. Stuyts, “Battery hybrid energy storage systems for full-electric marine applications,” *Processes*, vol. 10, no. 11, p. 2418, 2022. [Online]. Available: https://www.mdpi.com/2227-9717/10/11/2418

[13] W. Vermeer, G. R. C. Mouli, and P. Bauer, “A comprehensive review on the characteristics and modeling of lithium-ion battery aging,” *IEEE Transactions on Transportation Electrification*, vol. 8, no. 2, pp. 2205–2232, 2021. [Online]. Available: https://ieeexplore-ieee-org.tudelft.idm.oclc.org/abstract/document/9662298

[14] “Lithium ion battery vector illustration.” [Online]. Available: https://www.dreamstime.com/lithium-ion-battery-vector-illustration-labeled-explanation-energy-scheme-charging-graphic-cath
res5606696

[15] N. Nitta, F. Wu, J. T. Lee, and G. Yushin, “Li-ion battery materials: present and future,” *Materials today*, vol. 18, no. 5, pp. 252–264, 2015. [Online]. Available: https://www-sciencedirect-com.tudelft.idm.oclc.org/science/article/pii/S1369702114004118

[16] H.-J. Kim, T. Krishna, K. Zeb, V. Rajangam, C. V. M. Gopi, S. Sambasivam, K. V. G. Raghavendra, and I. M. Obaidat, “A comprehensive review of li-ion battery materials and their recycling techniques,” *Electronics*, vol. 9, no. 7, p. 1161, 2020. [Online]. Available: https://www.mdpi.com/2079-9292/9/7/1161

[17] S. A. Langevin, C. A. McHale, T. Hamann, and J. S. Ko, “Systematic design of safe, high-energy lithium-ion batteries by merging intercalation and alloying anodes,” *Journal of Materials Chemistry A*, vol. 13, no. 33, pp. 27 093–27 100, 2025. [Online]. Available: https://pubs.rsc.org/en/content/articlehtml/2025/ta/d5ta05287d

[18] T.-F. Yi, L.-J. Jiang, J. Shu, C.-B. Yue, R.-S. Zhu, and H.-B. Qiao, “Recent development and application of li4ti5o12 as anode material of lithium ion battery,” *Journal of Physics and Chemistry of Solids*, vol. 71, no. 9, pp. 1236–1242, 2010. [Online]. Available: https://www-sciencedirect-com.tudelft.idm.oclc.org/science/article/pii/S0022369710001526

[19] J. Vetter, P. Novák, M. R. Wagner, C. Veit, K.-C. Möller, J. Besenhard, M. Winter, M. Wohlfahrt-Mehrens, C. Vogler, and A. Hammouche, “Ageing mechanisms in lithium-ion batteries,” *Journal of power sources*, vol. 147, no. 1-2, pp. 269–281, 2005.

[20] J. S. Edge, S. O’Kane, R. Prosser, N. D. Kirkaldy, A. N. Patel, A. Hales, A. Ghosh, W. Ai, J. Chen, J. Yang *et al.*, “Lithium ion battery degradation: what you need to know,” *Physical Chemistry Chemical Physics*, vol. 23, no. 14, pp. 8200–8221, 2021. [Online]. Available: https://pubs-rsc-org.tudelft.idm.oclc.org/en/content/articlehtml/2021/cp/d1cp00359c

[21] J. Schmalstieg, S. Käbitz, M. Ecker, and D. U. Sauer, “A holistic aging model for li (nimnco) o2 based 18650 lithium-ion batteries,” *Journal of power sources*, vol. 257, pp. 325–334, 2014. [Online]. Available: https://www-sciencedirect-com.tudelft.idm.oclc.org/science/article/pii/S0378775314001876?casa_token=l5knzP5RWswAAAAA:sCQucl8-Zz4cu_RFYPfhRTNT8--2MHA5pzZrlwOdRxZSqoD1fQgi9LCGKPTkLp5TLviD51LmhpPh

[22] M. Schimpe, M. E. von Kuepach, M. Naumann, H. C. Hesse, K. Smith, and A. Jossen, “Comprehensive modeling of temperature-dependent degradation mechanisms in lithium iron phosphate batteries,” *Journal of The Electrochemical Society*, vol. 165, no. 2, p. A181, 2018. [Online]. Available: https://iopscience.iop.org/article/10.1149/2.1181714jes/meta#s1

[23] G. Zubi, R. Dufo-López, M. Carvalho, and G. Pasaoglu, “The lithium-ion battery: State of the art and future perspectives,” *Renewable and sustainable energy reviews*, vol. 89, pp. 292–308, 2018. [Online]. Available: https://www.sciencedirect.com/science/article/pii/S1364032118300728?casa_token=bc-TkNuB1UAAAAAA:5gXpqLmZFRAmKxuHQ4C-SzWKUDRyYjo-UdAm33TvXXmEoyzH8_YhXfnS-ia-SGmbe2iH6R7mzqY

[24] YuliyaPreger. *et al.*, “Degradation of commercial lithium-ion cells as a function of chemistry and cycling conditions,” *Journal of The Electrochemical Society*, 2020. [Online]. Available: https://iopscience-iop-org.tudelft.idm.oclc.org/article/10.1149/1945-7111/abae37/meta

[25] “Lithium-ion battery cell prices by chemistry,” *ourworld in data*, 2025. [Online]. Available: https://ourworldindata.org/grapher/average-battery-cell-price?country=LFP~NMC

[26] “Lithium titanate oxide battery market size share analysis - growth trends and forecast (2025 - 2030) source: https://www.mordorintelligence.com/industry-reports/lithium-titanate-oxide-battery-market,” *Mordor intelgance*, 2025.

[Online]. Available: https://www.mordorintelligence.com/industry-reports/lithium-titanate-oxide-battery-market

[27] X. Zeng, J. Li, and N. Singh, “Recycling of spent lithium-ion battery: A critical review,” *Journal of Power Sources*, vol. 259, pp. 276–302, 2014. [Online]. Available: https://www.tandfonline.com/doi/full/10.1080/10643389.2013.763578?casa_token=nZwQywx-8yAAAAAA%3Ape9JK6NqTfsMjezCufl6ZahZzWlwY_20MH6flRJJaYkOKHOBCIDNI3bNtf-Ow33ATTyXZcR2MxX0Gg#d1e117

[28] ufinebattery, “Nmc vs. lfp vs. lto batteries: A complete comparison guide,” *ufinebattery*, 2025. [Online]. Available: https://www.ufinebattery.com/blog/nmc-vs-lfp-vs-lto-batteries-a-complete-comparison-guide/?utm_source=chatgpt.com

[29] T. Nemeth, P. Schröer, M. Kuipers, and D. U. Sauer, “Lithium titanate oxide battery cells for high-power automotive applications–electro-thermal properties, aging behavior and cost considerations,” *Journal of Energy Storage*, vol. 31, p. 101656, 2020. [Online]. Available: https://www.sciencedirect.com/science/article/pii/S2352152X20314936?casa_token=cP8EtXsy7fsAAAAA:KyJByvv757K7JbeBjbdpXJXNJZ0zXAfRbFb8xJOu36NXYAF1wny--dOgKdSKuQIJJO1e8WPGWJ8

[30] J. de Hoog, J.-M. Timmermans, D. Ioan-Stroe, M. Swierczynski, J. Jaguemont, S. Goutam, N. Omar, J. Van Mierlo, and P. Van Den Bossche, “Combined cycling and calendar capacity fade modeling of a nickel-manganese-cobalt oxide cell with real-life profile validation,” *Applied Energy*, vol. 200, pp. 47–61, 2017. [Online]. Available: https://www-sciencedirect-com.tudelft.idm.oclc.org/science/article/pii/S0306261917305251?casa_token=8VE7TYZuIZQAAAAA:gJZ8febV6rRSVWECzXuEAdOFG1woUUYIgtcRv1Ex07bBzDGQe4AxWhsloPVkeRbb4dapo3g53Ys

[31] M. Soltani, J. Ronsmans, and J. Van Mierlo, “Cycle life and calendar life model for lithium-ion capacitor technology in a wide temperature range,” *Journal of Energy Storage*, vol. 31, p. 101659, 2020. [Online]. Available: https://www-sciencedirect-com.tudelft.idm.oclc.org/science/article/pii/S2352152X20314961?casa_token=TBkjkRhwKNgAAAAA:pDfIFVrfD5GQ2p3fX5TnJ0Cc_OjXkEd3iERg2ezPAnJeLOsIiNkclebODZGAC04OLRIXy8Tcfoc

[32] S. Prasad, “Empirical battery degradation modelling similarities, differences and shortcomings of various models,” *TU DELFT*, 202. [Online]. Available: https://repository.tudelft.nl/record/uuid:d9a1260f-1550-4bdf-be79-03d97632e6e5